Journal of Natural Gas Science and Engineering 49 (2018) 94–109

Contents lists available at ScienceDirect

Journal of Natural Gas Science and Engineering

journal homepage: www.elsevier.com/locate/jngse

Evolution of permeability during the process of shale gas extraction

Guanglei Cui[a,b], Jishan Liu[c,*], Mingyao Wei[a], Xiating Feng[a], Derek Elsworth[d]

[a] State Key Laboratory of Geomechanics and Geotechnical Engineering, Institute of Rock and Soil Mechanics, Chinese Academy of Sciences, Wuhan 430071, China
[b] University of Chinese Academy of Sciences, Beijing 100049, China
[c] School of Mechanical and Chemical Engineering, The University of Western Australia, 35 Stirling Highway, Perth, WA 6009, Australia
[d] Department of Energy and Mineral Engineering, G3 Center and Energy Institute, The Pennsylvania State University, University Park, PA 16802, USA

ARTICLE INFO

Keywords:
Shale permeability
Matrix heterogeneity
Mass transfer
Stress transfer
Strain evolution

ABSTRACT

The sensitivity of shale permeability to effective stress has been reported widely in the literature but the relation between them is not always consistent with the principle of effective stress. This knowledge gap defines our specific research goals: (1) to resolve the inconsistency between the evolution of shale permeability and the effective stress principle, and (2) to incorporate the evolution of shale permeability into the evaluation of shale gas production rate. In this study, we define shale blocks bounded by artificially introduced hydraulic fractures. At block scale the system comprises two components represented by inorganic and organic components. Unlike previous studies, we assume that the organic system is embedded within the inorganic system and both systems are dual porosity media. We define the shale permeability as a function of strains representing the stress transfer between fractures and matrix. These permeability-strain relations (shale permeability models) are then used to couple the governing equations of shale deformation and gas flow. The composite suite of equations are then solved by a commercial PDE solver. We use the coupled model to generate typical evolution profiles of shale permeability under stress-controlled conditions for the cases of both gas injection and gas desorption. These profiles are consistent with experimental observations as reported widely in the literature. We also use the coupled model to examine how the shale permeability evolves during the extraction of shale gas. Model results show that the evolutions of both shale permeability and gas production rate at field scale are primarily controlled by the contrasts in both the transport and deformation properties of the reservoir and the interfacial dynamics of mass and effective stress transfer between matrix and fractures.

1. Introduction

Shale gas has become an important component in the world energy mix due to its abundance, utility and corresponding reduced carbon intensity over other fossil fuels (Saghafi et al., 2007; Bai et al., 2013; Vafaie et al., 2015). Although a number of studies have been conducted to investigate the key processes of shale gas extraction, from nano-scale to field-scale, two major questions remain unresolved. At experimental scales, it has been observed that shale permeability is extremely sensitive to effective stress. However, the relation between shale permeability and effective stress is not well understood. At field scales, sharp decreases in gas production rate are normally observed following initial production, and these observations have led to uncertainties in the gas production forecast. However, the relation between the evolution of shale permeability and the sharp decrease of shale gas production rate has not been fully addressed.

At experimental scales, previous studies have demonstrated that shale permeability is extremely sensitive to effective stress. Kumar et al. (2015) conducted a series of experiments on intact and fractured shale samples to investigate permeability evolution and found that the permeability exhibited a two-stage evolution with gas pressure during the injection process of CO_2. Permeability first decreased as gas pressure was increased, reached a minimum close to double the Langmuir pressure (at 3.5 MPa), and then rebounded as the gas pressure was further increased. A stress-based permeability model (Kumar et al., 2012) was used to explain the observations. However, the model could not fully explain the observations. Similar experiments examined desorption (Jin et al., 2015) showed that the permeability would increase during desorption of N_2 under a constant confining stress and decreased pore pressure. In this work, the permeability increase was attributed to the Klinkenberg effect or slip-flow effect at low pore pressures. In both studies, the effective stress decreases as the gas pressure increases. This reduction in effective stress would increase the permeability based on the effective stress principle. Apparently, this theoretical conclusion is inconsistent with both experimental observations. In both studies, the strain caused by adsorption and the interaction between different

* Corresponding author. School of Mechanical and Chemical Engineering, The University of Western Australia, 35 Stirling Highway, Perth, WA 6009, Australia.
E-mail address: jishan.liu@uwa.edu.au (J. Liu).

https://doi.org/10.1016/j.jngse.2017.10.018
Received 25 November 2016; Received in revised form 24 September 2017; Accepted 31 October 2017
Available online 04 November 2017
1875-5100/

process components were not considered. Chen et al. (2015c) studied the strain behavior due to two gases (helium and methane) and demonstrated the significance of the adsorption-induced strain in shale. Heller and Zoback (2014) measured methane and carbon dioxide adsorption isotherms at 40 °C on gas shale samples and showed that the adsorption swelling was approximately linearly proportional to the adsorption mass. These studies may suggest that the inconsistency between the experimental permeability and the effective stress principle may be related to the gas sorption-induced strain.

At field scales, a number of studies have been conducted to investigate the impact of shale structures on gas production. A mathematical model was developed by Akkutlu and Fathi (2012) to analyze multi-scale gas flow in organic-rich shale with three different components: organic matrix, inorganic matrix and natural fractures. Gas transport followed a sequential approach in which the organic matrix (kerogen) communicated the natural fractures with the inorganic matrix. Hudson et al. (2012) introduced multiple porosity systems including systems in series with cross-flow or exchange and in parallel. Haghshenas et al. (2013) investigated gas flow in shales under three conditions: (i) including organic matrix and fractures only, inorganic/organic matter contributing to the fractures both (ii) simultaneously and (iii) in sequence. These studies have focused on the heterogeneous structure of the inorganic system, however, the organic system also exhibits a heterogeneous structure (Ambrose et al., 2010; Naraghi and Javadpour, 2015) but the impacts of this have been only sparingly explored. Some studies have shown that the inorganic system primarily determines the shale flow behavior while the organic system determines the gas storage (Ho et al., 2016; Lee et al., 2016). In fact, the organic system is embedded in the inorganic system and the organic system communicates with the hydraulic fracture only *via* the inorganic system, both through mass exchange and stress transfer. The nature of the high physical property contrasts between the two systems determines that both the mass transfer and the stress transfer between the two systems are the limiting processes for shale gas production. The process of mass transfer is well studied while stress transfer, and the coupling behavior between these two, are seldom the focus of study. From this brief review, it can be concluded that the structural characteristics of shale exert a significant impact on gas production processes at field scales.

However, the relation between the evolution of shale permeability at experimental scales and the sharp decrease of shale gas production rate at field scales has also not been fully addressed. As pore diameters in shale reservoirs are much smaller than those in conventional reservoirs, the concept of continuum flow theory may no longer hold (Sherman, 1969) and the concept of intrinsic permeability may not directly apply. Alternatively, the concept of apparent permeability has been used (Javadpour, 2009). The apparent permeability is written as the product of a correction factor and intrinsic permeability, commonly shown as: $k = f(Kn)k_\infty$ (Civan, 2009). $f(Kn)$ represents the correction factor which is often related to the Knudsen number (Kn), and k_∞ represents the intrinsic permeability which depends on the pore structure.

The correction factor $f(Kn)$ (shown in Table 1) has been extensively studied in porous media while the intrinsic permeability variation with mass transfer and stress transfer during gas production is rarely studied. Throughout production, the gas pressure in both the inorganic and organic systems changes and a contrast in pressures between fractures and matrix is created. As production progresses, the matrix pressure decreases while the effective stress in the matrix increases. The zone of stress influence expands from the fracture wall into the matrix. The impact of stress transfer in the expansion zone on the evolution of shale permeability is reflected in the intrinsic permeability (k_∞) model. Bustin et al. (2008) illustrated the relationship of shale permeability with effective stress and found that permeability varied by several orders of magnitude with effective stress. Chen et al. (2015a) established a theoretical model describing the relationship between fracture permeability and effective stress, and showed that fracture permeability would decrease significantly with gas depletion. These models were developed either for artificial fractures or artificially separated natural fractures (Carey et al., 2015) and the impact of stress transfer was ignored. Liu et al. (2011) proposed a mechanistic model in which the permeability was controlled by the switching of processes between local-swelling and macro-swelling. The incorporation of such processes in the evolution of shale permeability, and their impact on shale gas production, have been only sparingly reported in the literature. Peng et al. (2014) presented a new permeability model to explain such experimental observations of permeability evolution, and extended this to shale gas reservoirs (Peng et al., 2015). These previous studies focused exclusively on the dependence of shale permeability on effective stress, not on the effective stress transfer between organic and inorganic components within a single shale block.

The specific goals of this study are (1) to address the inconsistency between the evolution of shale permeability and the effective stress principle, and (2) to investigate the relation between the evolution of shale permeability and the sharp decrease of shale gas production rate. In order to achieve these goals, we define the shale permeability as a function of strains representing the stress transfer between fractures and matrix instead of the effective stress itself. These permeability-strain relations (shale permeability models) are then used to couple the governing equations of shale deformation and gas flow. The composite suite of equations are solved by a commercial PDE solver. The model is used to generate a typical four-stage evolution of shale permeability under conditions of stress-control. The model is also applied to explore why shale gas production rate decreases sharply after a relatively short period of high production. This approach and results are reported in the following sections.

2. Conceptual model

2.1. Two component systems

The hydraulic fracture is the essential step to the exploration of shale reservoir due to its ultra-low permeability, typically six orders of magnitude below that of conventional reservoir. A mount of hydraulic fluid, opponents and activators are injected into shale reservoir along well hole. Once the fracturing pressure large than formation strength, the hydraulic fracture appears along the direction of maximum principal stress. The exploration process of shale gas are seen in Fig. 1 (a). In this study, we define shale blocks bounded by artificially introduced hydraulic fractures. At block scale, the system comprises two components represented by inorganic and organic systems. Unlike previous studies, we assume that the organic system is embedded within the inorganic system and both systems are dual media. For these dual systems, there exist two boundaries: one is the interface between the two components, defined as the inner boundary, and the other is the shale block boundary called the outer boundary. The shale block exhibits highly heterogeneous properties of the mineral constituents, pore structure and gas storage, as observed in field emission scanning electron microscopy (FESEM) (Chen et al., 2013a; Mehmani et al., 2013). Fig. 1 (a) presents a typical high resolution SEM image of shale (Ambrose et al., 2010; Akkutlu and Fathi, 2012; Wasaki and Akkutlu, 2014). The organic (kerogen) and inorganic components are well resolved as dark- and light-grey regions, respectively. Laminar slit-shaped pores are also apparent in the inorganic system. In addition, a collection of organic inclusions are distributed in the shale with the existence of a sponge-like structures and with well-developed complex and interconnected nanopores (Ambrose et al., 2010; Curtis et al., 2012; Yang et al., 2016). As the majority of the gas is stored in the organic system, which is characterized within the heterogeneous structure (including organic pores and kerogen matrix), it is necessary to further subdivide the organic system, as shown in Fig. 1 (b) (Shi et al., 2015). The red, dark grey and light grey (Fig. 1(b)) represent the organic systems pores, kerogen and inorganic minerals, respectively. Note that the slit-shaped pores in the inorganic matrix may not even be appear in these small-scale images because of their large size. For further simplification, the

Table 1
The summary of $f(Kn)$ expressions.

$f(Kn)$ expression	Author(s)	$f(Kn)$ expression	Author(s)
Klinkenberg correction			
$f = \left(1 + \frac{b_k}{\bar{p}}\right)$	Klinkenberg (1941)	$b_k = 13.951\left[\frac{k_\infty}{\phi}\right]^{-0.53}$	Sampath and Keighin (1982)
$b_k = 11.419(k_\infty)^{-0.39}$	Heid et al. (1950)	$b_k = p\frac{4Kn}{1+Kn} + p\alpha(Kn)\left(1 + \frac{4Kn}{1+Kn}\right)$	Li et al. (2014)
$b_k = 12.639(k_\infty)^{-0.33}$	Jones and Owens (1980)	$b_k = 4\mu_g\sigma\sqrt{\frac{\pi RT\phi}{2Mk}}$	Guo et al. (2015)
Slip flow correction			
$f(Kn) = 1 + \frac{4Kn}{1+Kn}$	Zhang et al. (2014)	$f(Kn) = 1 + 4\left(\frac{2-\xi_v}{\xi_v}\right)\frac{\lambda}{d}$	Sakhaee-pour and Bryant (2011)
$f(Kn) = 1 + 4.89Kn$	Chen et al. (2015b)	$f(Kn) = 1 + 4Kn$	Florence et al. (2007)
Transition correction			
$f(Kn) = 0.8453 + 5.4576Kn + 0.1633Kn^2$	Sakhaee-pour and Bryant (2011)	$f(Kn) = 1 + 6.85Kn + 3.39Kn^2$	Kazemi and Takbiri-Borujeni (2015)
Slip flow and Knudsen diffusion correction			
$f(Kn) = \frac{1+4.89Kn}{1+0.0006e^{Kn}} + \left(\frac{128\tau^2\mu_g\delta^2}{3\kappa\phi}\sqrt{\frac{\pi Rg}{MT}}\right)\left(\frac{0.0006e^{Kn}Kn}{1+0.0006e^{Kn}}\right)$		$f(Kn) = \frac{1+4.89Kn}{1+0.0024Kn^4} + \left(\frac{128\tau^2\mu_g\delta^2}{3\kappa\phi}\sqrt{\frac{\pi Rg}{MT}}\right)\left(\frac{0.0024Kn^4}{1+0.0024Kn^5}\right)$	Chen et al. (2015b)
Slip flow and Transition flow correction			
$f(Kn) = [1 + \alpha(Kn)Kn]\left[1 + \frac{4Kn}{1+Kn}\right]\alpha(Kn) = \frac{128}{15\pi^2}\tan^{-1}[4Kn^{0.4}]$			Florence et al. (2007)

organic system pores are treated as a connected domain combining the surrounding solid components and the kerogen is isolated by organic system pores as shown in Fig. 1 (b). It is assumed that the kerogen communicates with the inorganic component through organic pores in both gas flow and mechanical deformation behaviors.

2.2. Gas flow behavior

In this study, the gas in the organic/inorganic pores is treated as free gas while the gas on the organic pore surface and in the kerogen is treated as adsorbed gas, as shown in Fig. 1 (b). For free gas, the flow regimes are distinguished by the Knudsen number. The Knudsen number, Kn, defined as the ratio of the molecular mean free path to the pore diameter (Mulder, 1996), is a widely recognized dimensionless parameter determining the degree of appropriateness of the continuum flow model.

The variations of the Knudsen number and flow regime with pore diameter are presented in Fig. 2 (Javadpour et al., 2007). For the free gas in the inorganic pores, whose diameter ranges from several hundred nanometers (nanopores) to several micrometers (natural fractures), the flow regimes are mainly slip flow (seldom continuum flow). For the free gas in the organic pores, whose diameter is ~10 nm, the flow regime is also one of slip flow. The absorbed gases are transported due to the concentration gradient. A Langmuir model (Bumb and McKee, 1988) is used to define the adsorption process while the gas flow in the kerogen and on the organic pore surface is defined by diffusion.

2.3. Mechanical deformation behavior

In this section, we use gas injection as an example to illustrate the relation between effective stress and permeability evolution. Before injection, the sample is at an equilibrium state and the gas pressure is everywhere uniform. The injection process can be summarized in three stages: (1) Filling up the Inorganic System. As the gas is injected into the shale sample, the inorganic system fills with gas near-instantaneously because of its high permeability. The inorganic system would swell, leading to a larger pore aperture while the pore in the organic system would shrink. The permeabilities in these two systems exhibit opposite behaviors because of the heterogeneous distribution of local stress. The interface between these two systems during this stage (B_I) is shown in Fig. 3 (I); (2) Filling up the Organic Pores. As the injection continues, the gas flows into the organic pores. This situation is more complex than before as the organic pore not only stores free gas but also adsorbs gas. The adsorption-induced strain and the increased gas pressure in the organic system resists the compressive stress applied by the inorganic system. In this stage, the inorganic system shrinks and the location of the new interface (B_{II}) is determined by the interactions between the organic pore pressure, adsorption-induced stress and compressive stress applied by the inorganic system as shown in Fig. 3 (II); (3) Reaching a New Equilibrium State. In the final stage, the gas diffuses into the solid component of the organic system (kerogen). Similarly, the organic pores are compressed and the kerogen swells due to the gas adsorption onto the kerogen. Also, the inorganic system is compressed because of the stress transfer during this stage. At the end of this process, the gas capacity is reached and the interface between the two systems is determined by the outer boundary. Two end-member boundary conditions are discussed here. If the control volume is retained at constant volume, the permeabilities of the inorganic and organic systems would decrease due to the swelling of the kerogen matrix as shown in Fig. 3 (III,a). If the unit is constrained at constant pressure/stress, P, the control volume would swell as shown in Fig. 3 (III,b). In this situation, the permeabilities of the inorganic and organic systems are determined by the evolution of the global swelling strain and the local compressive strain.

There are two boundaries present in the shale block: one is the interface between the inorganic and organic systems (inner boundary) and the other is the shale block boundary (outer boundary). Three special mechanical situations are discussed as follows: (1) when the modulus of the inorganic system is infinite and the embedded organic component is deformable, then the strain for the inorganic system is zero while the organic system conforms to the constant volume condition. In this situation, the matrix behavior is mainly controlled by the internal boundary. Clearly, as gas is released the kerogen shrinks and the organic pores swell while the inorganic pores remain unchanged; (2) when the modulus of the inorganic system approaches zero, the inorganic component is free to deform while the organic component is elastic. Both the porosity and permeability behaviors are controlled by the outer boundary; (3) when the moduli of the two systems are equal, the inorganic system can be seen as the extension of the organic system in mechanical behavior. In this situation, the porosity and permeability behaviors are controlled by both inner and outer boundaries. For the field situation, the modulus of the inorganic system is typically larger than that of the organic system. Thus, the porosity and permeability behaviors are closer to the constant volume response. The three special conditions are illustrated in Fig. 4.

3. Model formulations

In this section, the conceptual model discussed above is formulated and the equations governing the mechanical deformation of shale, gas flow in both components, mass transfer and the evolution of

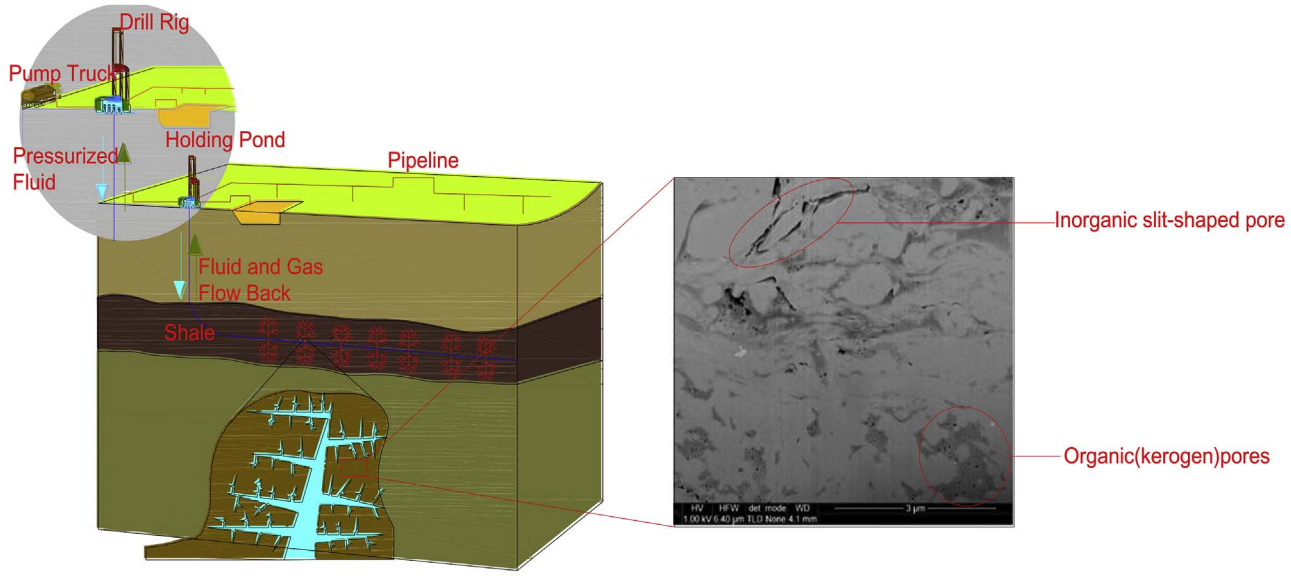

(a) Exploration process for shale gas recovery and SEM image of shale matrix (Ambrose et al., 2010; Akkutlu and Fathi, 2012; Wasaki and Akkutlu, 2014);

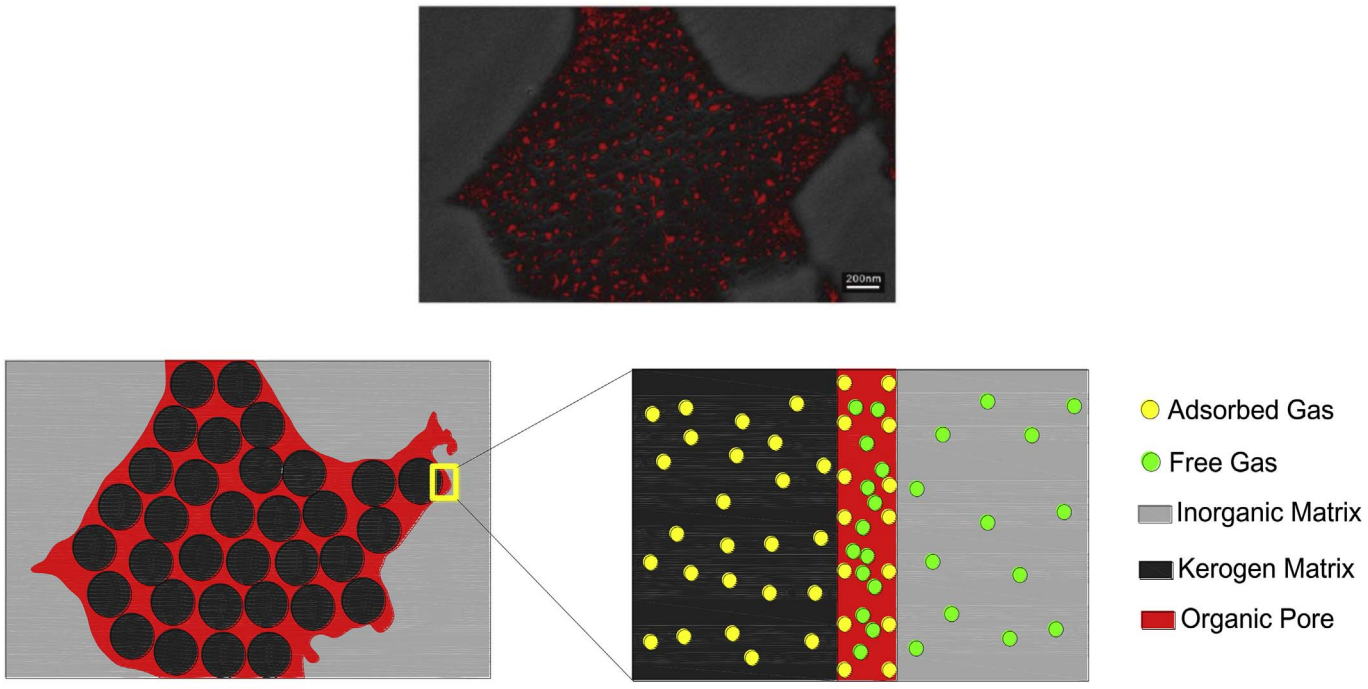

(b) The heterogeneous of shale matrix (Shi et al., 2015)

Fig. 1. Illustration of shale matrix system.

permeability are established. The global strain and local strain defined in Peng's work (2014) are referenced. In our work, the subscript *e* represents the effective strain, subscript *g* represents the global strain and local strain is represented by subscript *l*.

3.1. Governing equation of the mechanical process

Similar to the mechanical relations for dual porosity media (Zhang et al., 2008; Wu et al., 2011), considering the influences of pore pressure and adsorption-induced strain, the constitutive deformation for the shale reservoir becomes:

$$Gu_{i,kk} + \frac{G}{1-2v}u_{k,ki} = f_i + \alpha_{in}p_{in,i} + \alpha_{or}p_{or,i} + \alpha_{ke}p_{ke,i} + K\varepsilon_{s,i}(p_{or}) + K\varepsilon_{s,i}(p_{ke}) \quad (1)$$

where u is the displacement, p is the gas pressure, ε_s is the sorption

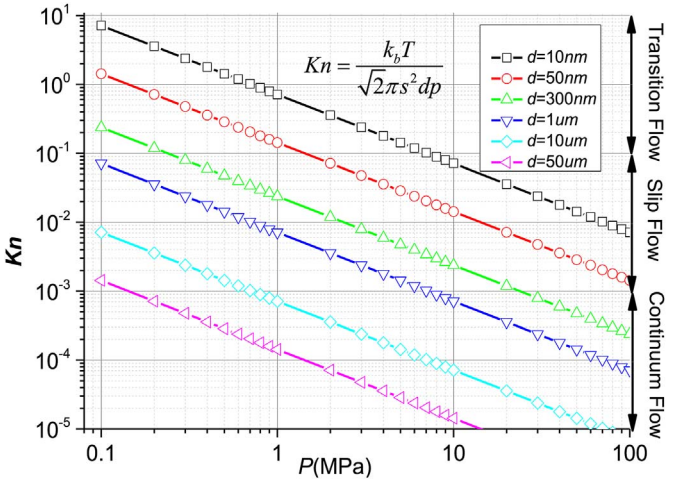

Fig. 2. Relationship between the Knudsen number and gas pressure for different pore diameters, where k_b is the Boltzmann constant, T is the temperature in shale reservoir, s is the collision diameter for molecules (Javadpour et al., 2007).

strain, α is the Biot coefficient, K is the bulk modulus and G is the shear modulus. The subscripts *in*, *or* and *ke* represent the inorganic system, organic pore and kerogen matrix, respectively. The subscripts i and k represent the directional component of the variable in which$i$, k = 1,2,3, the subscript *kk* is the Einstein summation convention and the subscript comma represents the derivative of a variable.

The gas adsorption-induced strain is obtained from the Langmuir equation:

$$\varepsilon_s = \frac{\varepsilon_L p}{P_L + p} \tag{2}$$

where ε_L is the Langmuir strain constant and P_L is the Langmuir pressure constant.

3.2. Governing equations of the flow processes

3.2.1. Flow in inorganic system

As mentioned above, the flow regime in the inorganic system can be described by slip flow and the correction factor $f_{in}(Kn) = 1 + \frac{4Kn_{in}}{1+Kn_{in}}$, is selected in this work. The mass conservation law for flow in the inorganic system is defined as:

$$\frac{\partial m_{in}}{\partial t} + \nabla \cdot J_{in} = Q_{in-or} + Q_s \tag{3}$$

where J_{in} is the mass flux of gas transport in the inorganic minerals, Q_s is the mass source term and $Q_{in\text{-}or}$ is the mass transfer between inorganic pores and organic pores. m_{in} represents the gas mass in the inorganic system and only free gas exits:

$$m_{in} = \rho_{in}\phi_{in} \tag{4}$$

whereϕ_{in} is the inorganic porosity and ρ_{in} is the gas density in the inorganic system. The J_{in} is the mass flux in the form of a pressure gradient defined as a modified Darcy equation:

$$J_{in} = -\frac{k_{apin}}{\mu}\rho_{in}\nabla p_{in} \tag{5}$$

where μ is the dynamic viscosity of gas and k_{apin} is the apparent permeability of the inorganic system which can be expressed as:

$$k_{apin} = \left(1 + \frac{4Kn_{in}}{1 + Kn_{in}}\right)k_{in\infty} \tag{6}$$

in which $k_{in\infty}$ is the intrinsic permeability of the inorganic system.

3.2.2. Flow in organic system

The mass conservation law for the organic pore is defined as:

$$\frac{\partial m_{or}}{\partial t} + \nabla \cdot J_{or} = -Q_{in-or}. \tag{7}$$

The gas mass content m_{or} contains free-phase gas and absorbed gas in the organic pore as well as the mass source term from the kerogen, and is defined as:

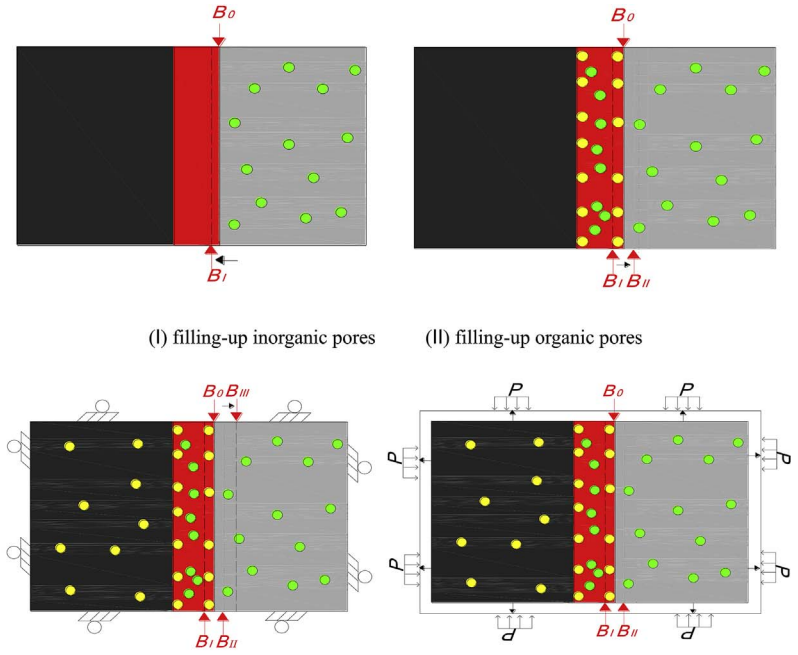

(I) filling-up inorganic pores (II) filling-up organic pores

(III,a) diffusing into kerogen under constant volume condition (III,b) diffusing into kerogen under constant stress condition

Fig. 3. Illustration of gas injection processes, *B* presents the internal boundary between inorganic and organic systems, subscripts *0,I,II,III* represent the location at the initial stage, the first stage, the second stage and the third stage, and the arrow represents the displacement direction of the boundary during this stage.

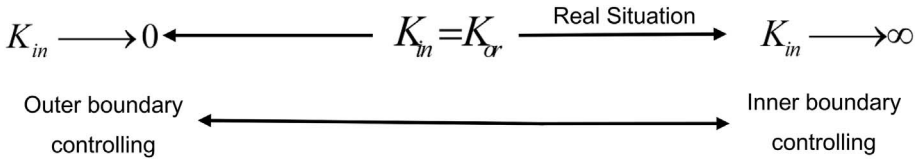

Fig. 4. Illustration of relation between the contrast in modulus magnitudes between inorganic and organic systems and the controlling degree of boundary conditions.

$$m_{or} = \rho_{or}\phi_{or} + \phi_{or}\rho_{ga}\rho_{ors}\frac{V_{Lor}p_{or}}{p_{or}+P_{Lor}} + \phi_k\rho_{ga}\rho_k m_{ke} \tag{8}$$

where ϕ_{or} is the organic pore porosity, ϕ_k is the kerogen proportion, P_{Lor} is the Langmuir pressure constant in the organic pore, V_{Lor} is the Langmuir volume constant in the organic pore, ρ_{ga} is the gas density at standard atmospheric pressure, ρ_{ors} is the density of the organic pore surface, ρ_{or} is the gas density in the organic pore and ρ_k is the density of kerogen.

The total mass flux in the organic pores is the combination of the slip flow term and surface diffusion term, and is defined as:

$$J_{or} = J_{orslip} + J_{orsur} \tag{9}$$

where the first term represents the mass flux from slip flow and the second term represents the mass flux from surface diffusion. The slip flow term is written as a modified Darcy flow:

$$J_{orslip} = -\frac{\rho_{or}k_{or\infty}}{\mu}\left(1+\frac{4Kn_{or}}{1+Kn_{or}}\right)\nabla p_{or} \tag{10}$$

where $k_{or\infty}$ is the intrinsic permeability of the organic system. And the surface diffusion term is defined as:

$$J_{orsur} = -D_{or}\nabla C_{or} \tag{11}$$

where D_{or} is the surface diffusivity in the organic system and C_{or} is the gas concentration in the organic system. The Langmuir equation is applied to obtain the concentration as:

$$C_{or} = \rho_{ga}\rho_{ors}\frac{V_{Lor}p_{or}}{p_{or}+P_{Lor}}. \tag{12}$$

The total mass flux can also be written in the form of apparent permeability:

$$J_{or} = -\frac{k_{apor}}{\mu}\rho_{or}\nabla p_{or} \tag{13}$$

where k_{apor} is the apparent permeability of organic pore and can be expressed as:

$$k_{apor} = k_{or\infty}\left(1+\frac{4Kn_{or}}{1+Kn_{or}}\right) + D_{or}\rho_{ga}\rho_k\frac{V_{Lor}p_{Lor}}{(p_{or}+P_{Lor})^2}\frac{\mu}{\rho_{or}}. \tag{14}$$

3.2.3. Mass transfer term

The gas mass transfer between the inorganic and organic systems is determined by the gas content difference. The mass transfer is proportional to the gas pressure (Lim and Aziz, 1995):

$$Q_{in-or} = \frac{\sigma_{or}k_{apor}}{\mu}\rho_{or}(p_{or}-p_{in}) \tag{15}$$

where σ_{or} is the shape factor in the organic system.

The mass transfer rate between kerogen and the organic system pores ($\phi_k\rho_{ga}\rho_k m_{ke}$) is defined by the diffusion time in the kerogen (Wang et al., 2012):

$$\frac{dm_{ke}}{dt} = -\frac{1}{\tau_{ke}}[m_{ke}-m_e(p_{wall})] \tag{16}$$

where $m_e(p_{wall})$ is the gas concentration in equilibrium with interface pressure p_{wall}. In this equation, the diffusion time in the kerogen is expressed as:

$$\tau_{ke} = \frac{1}{\alpha_{ke}D_{ke}} \tag{17}$$

where $D_{ke}(m^2/s)$ is the diffusion coefficient in the kerogen and α_{ke} is a shape factor in the kerogen matrix. In our work, the assumption of pseudo-steady state is made and the interface pressure p_{wall} is equal to the organic pore pressure p_{or}. The absorbed gas content at equilibrium $m_e(p_{wall})$ is calculated by the Langmuir isotherm:

$$m_e(p_{wall}) = \frac{V_{Lor}p_{or}}{P_{Lor}+p_{or}}. \tag{18}$$

In summary, the gas flow equations in shale are defined as:

(a) Gas flow in inorganic pores,

$$\frac{\partial(\rho_{in}\phi_{in})}{\partial t} + \nabla\cdot\left(-\frac{\rho_{in}}{\mu}k_{apin}\nabla p_{in}\right) = \frac{\sigma_{or}k_{apor}}{\mu}\rho_{or}(p_{or}-p_{in}) + Q_s \tag{19}$$

(b) Gas flow in organic pores,

$$\frac{\partial\left(\rho_{or}\phi_{or} + \phi_{or}\rho_{ga}\rho_{ors}\frac{V_{Lor}p_{or}}{p_{or}+P_{Lor}}\right)}{\partial t} + \nabla\cdot\left(-\frac{\rho_{or}}{\mu}k_{apor}\nabla p_{or}\right) = -\frac{\sigma_{or}k_{apor}}{\mu}\rho_{or}(p_{or}-p_{in}) + \phi_k\rho_{ga}\rho_k\frac{1}{\tau_{ke}}[m_{ke}-m_e(p_{wall})] \tag{20}$$

(c) Gas diffusion in kerogen,

$$\frac{dm_{ke}}{dt} = -\alpha_{ke}D_{ke}\left[m_{ke}-\frac{V_{Lor}p_{or}}{P_{Lor}+p_{or}}\right] \tag{21}$$

3.3. Permeability models

3.3.1. The intrinsic permeability model of the inorganic system

The porosity of the inorganic system is related to the effective strain (Peng et al., 2014) and defined as:

$$\frac{\phi_{in}}{\phi_{in0}} = 1 + \frac{\alpha_{in}}{\phi_{in0}}\Delta\varepsilon_{ine} \tag{22}$$

Where ϕ_{in0} is the initial porosity of inorganic matrix, the subscript, 0, denotes the initial value of the variable and ε_{ine} represents the effective strain in the inorganic system. The effective strain is the sum of the global strain and local strain of the inorganic system:

$$\Delta\varepsilon_{ine} = \Delta\varepsilon_{ing} + \Delta\varepsilon_{inl} \tag{23}$$

where the ε_{ing} represents the global strain in the inorganic system and ε_{inl} represents the local strain in the inorganic system. The global strain of the inorganic matrix is the resultant of the global strain of the shale block and the compressive strain applied by gas pressure and gas adsorption in organic system:

$$\Delta\varepsilon_{ing} = \Delta\varepsilon_v - \frac{(p_{or}-p_{in})}{K_{inm}} - f_{or2in}(\Delta\varepsilon_s(p_{or})) - f_{ke2in}(\Delta\varepsilon_s(p_k)) \tag{24}$$

where K_{inm} is the bulk modulus of the inorganic system The first term on the right represents the global strain of the shale reservoir, the second term represents the compressive strain applied by the organic system, and the last two terms represent the compressive strain applied by the adsorptive behavior of the organic pore and kerogen matrix, respectively. The local strain of the inorganic matter is applied by the

gas pressure in itself:

$$\Delta\varepsilon_{inl} = \frac{\Delta p_{in}}{K_{ins}} \tag{25}$$

where K_{ins} is the bulk modulus of the inorganic skeleton. A typical relationship between porosity and permeability is the cubic law (Zhang et al., 2008) and defined as:

$$\frac{k_{in\infty}}{k_{in\infty 0}} = \left(\frac{\phi_{in}}{\phi_{in0}}\right)^3 = \left(1 + \frac{\alpha_{in}}{\phi_{in0}}\Delta\varepsilon_{ine}\right)^3 \tag{26}$$

3.3.2. The intrinsic permeability model of organic system

Similarly, the porosity of the organic system is related to the effective strain:

$$\frac{\phi_{or}}{\phi_{or0}} = 1 + \frac{\alpha_{or}}{\phi_{or0}}\Delta\varepsilon_{ore} \tag{27}$$

where ε_{ore} represents the effective strain of the organic pore. The effective strain ε_{ore} also includes the global strain and local strain of the organic system:

$$\Delta\varepsilon_{ore} = \Delta\varepsilon_{org} + \Delta\varepsilon_{orl} \tag{28}$$

where the first term ε_{ing} represents the global strain of the organic pore and the second term represents the local strain of the organic pore. The global strain of the organic matter is the combination of the global strain of the shale reservoir and the compressive strain applied by the inorganic matter and kerogen:

$$\Delta\varepsilon_{org} = \Delta\varepsilon_V - \frac{p_{in} - p_{or}}{K_{inm}} - \frac{p_k - p_{or}}{K_{kem}} - f_{ke2or}(\Delta\varepsilon_s(p_k)) \tag{29}$$

where K_{kem} is the bulk modulus of the kerogen matrix. The first term on the right represents the global strain of shale reservior, the second and third terms represent the compressional strain applied by the organic system and the kerogen matrix, respectively, and the last term represents the adsorption effect applied by kerogen matrix.

The local strain of the organic matter only contains the adsorption strain in itself:

$$\Delta\varepsilon_{orl} = -f_{or2or}(\Delta\varepsilon_s(p_{or})) \tag{30}$$

Also the cubic law describes the relationship between permeability and porosity of the organic pores:

$$\frac{k_{or\infty}}{k_{or\infty 0}} = \left(\frac{\phi_{or}}{\phi_{or0}}\right)^3 = \left(1 + \frac{\alpha_{or}}{\phi_{or0}}\Delta\varepsilon_{ore}\right)^3 \tag{31}$$

As discussed above, the adsorption-induced stress occurs in the organic system and is transferred to the inorganic system. Thus the adsorption stress in the kerogen not only compresses the pores in the organic matter but also compresses the pores in the inorganic system (Wang et al., 2014). Here γ_{ke}, a distribution coefficient depending on the modulus of the two systems and the boundary condition, is introduced. Thus for $f_{ke2or}(\Delta\varepsilon_s(p_k))$, we obtain:

$$f_{ke2or}(\Delta\varepsilon_s(p_k)) = (1 - \gamma_{ke})\frac{\varepsilon_{Lke}p_{ke}}{P_{Lke} + p_{ke}} \tag{32}$$

in which P_{Lke} is the Langmuir pressure constant of the kerogen matrix and ε_{Lke} is the Langmuir strain constant of the kerogen matrix. And for $f_{ke2in}(\Delta\varepsilon_s(p_k))$, we have:

$$f_{ke2in}(\Delta\varepsilon_s(p_k)) = \gamma_{ke}\frac{\varepsilon_{Lke}p_{ke}}{P_{Lke} + p_{ke}} \tag{33}$$

Similarly the pores in the organic and inorganic systems are both affected by the adsorption strain in the organic pore, and γ_{or} is introduced here. In our work, the $f_{or2or}(\Delta\varepsilon_s(p_k))$ is written as:

$$f_{or2or}(\Delta\varepsilon_s(p_{or})) = (1 - \gamma_{or})\frac{\varepsilon_{Lor}p_{or}}{P_{Lor} + p_{or}} \tag{34}$$

In which ε_{Lor} is the Langmuir strain constant of the organic pore. For $f_{or2in}(\Delta\varepsilon_s(p_k))$, we have:

$$f_{or2in}(\Delta\varepsilon(p_{or})) = \gamma_{or}\frac{\varepsilon_{Lor}p_{or}}{P_{Lor} + p_{or}} \tag{35}$$

If the inorganic modulus is infinite, then $\gamma_{ke} = \gamma_{or} = 0$ and the matrix has to swell inside, compressing the pore.

In summary, the permeability models for both inorganic and organic systems are defined as:

$$\frac{k_{in\infty}}{k_{in\infty 0}} = \left(1 + \frac{\alpha_{in}}{\phi_{in0}}\left(\Delta\varepsilon_v - \frac{(p_{or} - p_{in})}{K_{inm}} - \gamma_{or}\frac{\varepsilon_{Lor}p_{or}}{P_{Lor} + p_{or}} - \gamma_{ke}\frac{\varepsilon_{Lke}p_{ke}}{P_{Lke} + p_{ke}} + \frac{\Delta p_{in}}{K_{ins}}\right)\right)^3 \tag{36}$$

$$\frac{k_{or\infty}}{k_{or\infty 0}} = \left(1 + \frac{\alpha_{or}}{\phi_{or0}}\left(\Delta\varepsilon_V - \frac{p_{in} - p_{or}}{K_{irm}} - \frac{p_k - p_{or}}{K_{orm}} - \left(1 - \gamma_{ke}\right)\frac{\varepsilon_{Lke}p_{ke}}{P_{Lke} + p_{ke}} - \left(1 - \gamma_{or}\right)\frac{\varepsilon_{Lor}p_{or}}{P_{Lor} + p_{or}}\right)\right)^3 \tag{37}$$

3.4. Cross couplings

The deformation equation (Eq. (1)) and the gas flow equations (Eq. (19) - Eq. (21)) describe the deformation of the shale matrix and the gas flow in both components. The interactions between shale deformation and gas flow are represented by the permeability models of Eq. (36) and Eq. (37). Fig. 5 graphically represents the fully coupled processes of this developed model. The gas flow in both components will change the effective stress in shale matrix and the adsorption/desorption process in organic system will also induce swelling/shrinkage of the matrix. These effects may modify the stress field and the deformation of the shale matrix. Conversely, the mechanical deformation will compact/dilate the pore space and thus revise the storage and transport properties of both components. The diffusion process in the kerogen supplies adsorbed gas to the gas flow in the organic pores and the mass transfer between the organic system and the inorganic system is controlled by the gas pressure. During the process of mass transfer, coupled with stress transfer, both the porosities and permeabilities in both

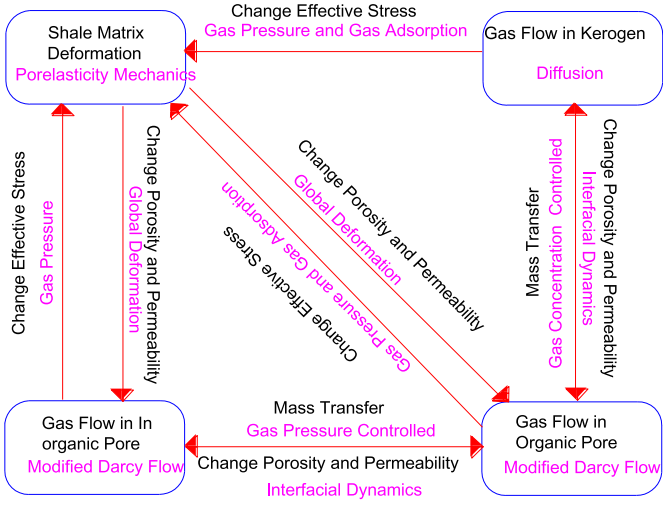

Fig. 5. Illustration of cross-couplings between variable processes within the inorganic and organic systems.

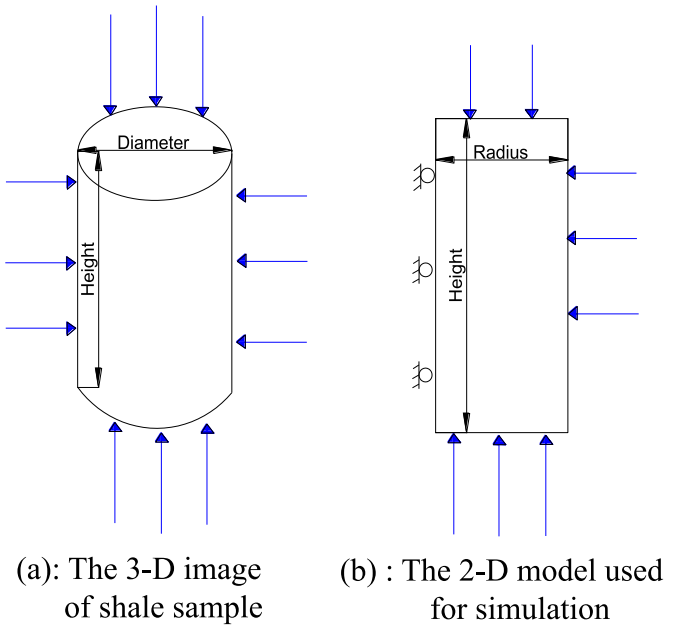

Fig. 6. Illustration of the simulation model.

components are modified because of the interfacial dynamics.

4. Analysis of experimental observations

4.1. Evolution of permeability under conventional tri-axial conditions

We use this coupled model to evaluate the evolution of permeability during the processes of gas injection and gas desorption under conventional tri-axial conditions. The shale sample is cylindrical and 2.5 cm in diameter and 5 cm in length, as shown in Fig. 6. The injection or desorption pressure, p_{gas}, is applied at the basal boundary of the inorganic system and a no flow boundary condition is applied to the other boundaries. The confining pressure, σ_{con}, is applied on all the boundaries and is kept constant. The initial gas pressure is p_0. The input parameters for the simulation are listed in Table 2.

Fig. 7 (a) shows the evolution of permeability during the gas injection process (p_0 = 1 MPa). Four distinct stages are observed: (1) Stage of Permeability Increase. Permeability increases in the early stage when the inorganic pores are filled with the injection gas immediately after the injection. This increase in permeability is due to the sudden increase in the injection pressure, concomitantly reducing effective stresses; (2) Stage of Permeability Decrease. Permeability decreases after the pressure in the inorganic pores reaches the injection pressure. At this stage, gas diffuses from the inorganic system into the organic system. Subsequently, the gas-invaded volume in the vicinity of the organic system swells and this swelling (local deformation) reduces the apertures of micro-fractures in the inorganic system. Therefore, the permeability in the inorganic system decreases; (3) Stage of Permeability Recovery. As the gas-invaded volume expands further into the organic system, the controlling factor on the evolution of permeability in the inorganic system switches gradually from the internal boundary to the external one. Only part of the swelling deformation contributes to the evolution of permeability; and (4) Stage of Permeability Stabilization. As the gas-invaded volume spreads throughout the organic system and a new equilibrium gas pressure between two systems is reached, the entire sample swells uniformly. Under this condition, permeability reaches its maximum value. This behavior is consistent with the results from coals (Chen et al., 2013b; Peng et al., 2014).

Results of permeability evolution for the desorption case are shown in Fig. 7 (b) (p_0 = 9 MPa). Similar to the case for gas injection, four distinct stages can also be observed: (1) Stage of Permeability Decrease. Permeability decreases in the early stage when the gas in the inorganic medium flows out immediately after the extraction. This reduction in permeability is due to the sudden decrease in the pressure in the inorganic system; (2) Stage of Permeability Increase. Permeability increases after the pressure in the inorganic pores reaches the extraction pressure. At this stage, gas diffuses from the organic system into the inorganic system. Subsequently, the gas-depleted volume in the vicinity of the organic system shrinks and this shrinkage (local deformation) dilates the micro-fractures in the inorganic system. Correspondingly, the permeability in the inorganic system increases; (3) Stage of Permeability Recovery. As the gas-depleted area expands further into the organic system, the controlling factor on the evolution of permeability in the inorganic system switches from the internal boundary to the external one. Only part of the shrinkage (deformation) contributes to the evolution of permeability; and (4) Stage of Permeability Stabilization. As the gas-depleted volume spreads throughout the organic system and a new equilibrium state between the inorganic system and the organic system is reached, the entire sample shrinks uniformly.

4.2. Comparison with experimental observations of gas injection

Kumar et al. (2015) investigated the injection and adsorption of gas (CO_2) on two intact samples of Marcellus shale under conditions of constant confining stress and variable gas pressure. The samples were cylinders 2.5 cm in diameter and 5 cm in length collected in Pennsylvania. The shale permeability evolution was investigated by injecting CO_2 into the intact core at a constant confining stress of 10 MPa and variable gas pressure increasing from 1 MPa to 6 MPa. The transient pulse test method was utilized to evaluate shale permeability (Brace et al., 1968). The values of k_{apin0} were 1.09×10^{-14} m^2 and 3.16×10^{-14} m^2 for samples A and B, respectively. For the simulation model, the injection pressure, p_{in}, is applied at the basal boundary of the inorganic system and no flow boundary conditions are applied on other boundaries. The confining pressure, 10 MPa, is applied on all the boundaries and kept constant. The input parameters for the simulation model are listed in Table 3 (Kumar et al., 2015). As shown in Fig. 8, the modeled results match well with the experimental observations.

4.3. Comparison with experimental observations of gas desorption

Jin et al. (2015) conducted experiments of gas desorption processes (N_2) on two intact samples under a constant confining stress. The two samples were cylinders of 2.5 cm diameter and, 2.1 cm and 1.2 cm length respectively, collected from North America. The gas pressure gradually decreased from 9 MPa to 4 MPa while the confining pressure was kept at 11 MPa. The complex pressure transient method (Boitnott, 1997; Siriwardane et al., 2009) was chosen to measure the gas shale permeability in this experiment. The values of k_{apin0} were 14.8×10^{-18} m^2 and 3.2×10^{-18} m^2 for sample BH and sample CH, respectively. For the simulation model, the depletion pressure, p_{de}, is

Table 2
Input parameters for the numerical example.

Simulation Scenario	ϕ_{in0}	k_{in0}	k_{or0}	E	ε_L	P_L
Adsorption	0.02	1×10^{-14} [m^2]	1.5×10^{-16} [m^2]	5[GPa]	0.07	3[MPa]
Desorption	0.01	1.5×10^{-17} [m^2]	1×10^{-19} [m^2]	40[GPa]	0.04	2[MPa]

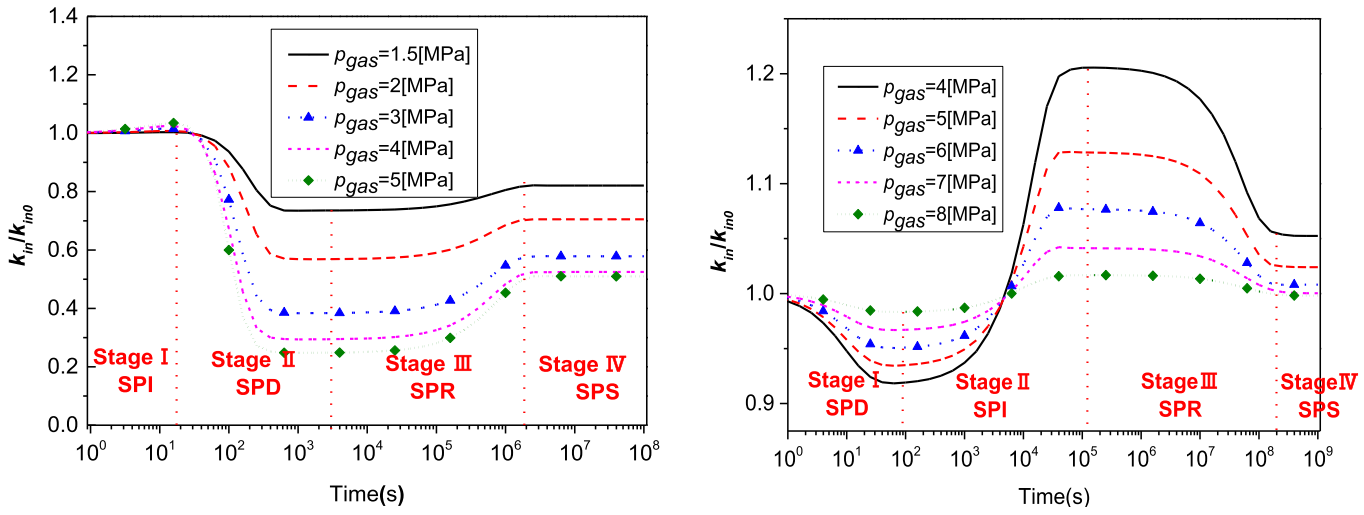

Fig. 7. Evolution of permeability during (a) injection and (b) desorption processes.

Table 3
Input parameters for the injection experiment conducted by Kumar et al. (2015).

Sample	ϕ_{in0}	k_{apin0}	k_{apor0}	E_{in}	ε_{Lor}	P_{Lor}
Sample A	0.02	1×10^{-14}[m^2]	1×10^{-16}[m^2]	5[GPa]	0.07	1.5[MPa]
Sample B	0.01	3×10^{-17}[m^2]	5×10^{-18}[m^2]	30[GPa]	0.03	1[MPa]

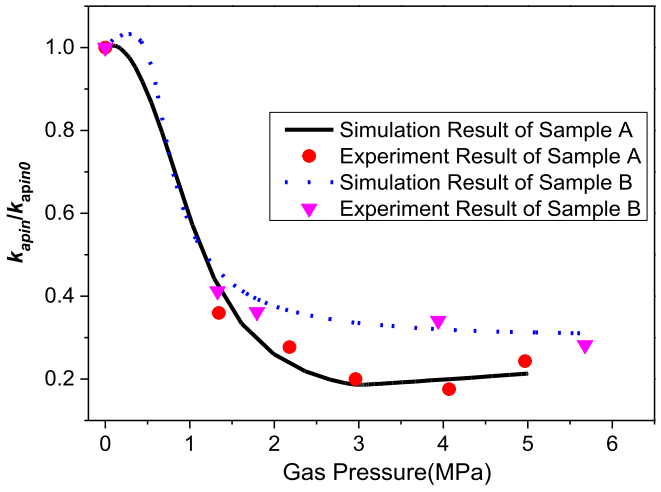

Fig. 8. Comparisons of modeled permeability with experimental data.

applied at the bottom boundary of the inorganic system and no flow boundary conditions are applied on the other boundaries. The confining pressure, 11 MPa, is applied on all the boundaries and kept constant. Other input parameters are listed in Table 4. As shown in Fig. 9, the modeled results match well with the experimental observations.

4.4. Discussions of matching results

When the confining stress is kept constant, the assumed effective stress in the samples decreases as the gas pressure increases for the case of injection while the assumed effective stress increases as the gas pressure decreases for the case of gas desorption. Therefore, the permeability should increase for the case of gas injection while the permeability should decrease for the case of gas desorption according to the effective stress principle. Based on this theoretical conclusion, only the experimental data of Sample CH (gas desorption) are consistent with the principle of effective stress - while the other three experiments contradict this principle. Conversely, our analysis matches all four of these cases. This superior match demonstrates that our coupled model has resolved the inconsistency between experimental observations and the effective stress principle. In our approach, both the contrast in permeability between different components and the swelling characteristics are important. The Langmuir strain constants for these cases are 0.07, 0.03, 0.002, and 0.0005, respectively. The case with the minimum Langmuir strain constant of 0.0005 (Sample CH, as shown in Fig. 9) is the only one case where the experimental data are consistent with the principle of effective stress. All others with larger Langmuir strain constants of 0.07, 0.03, and 0.002 contradict the principle. This indicates that the sorption-induced local strains control the permeability behavior. If local swelling is significant, the shale permeability is controlled primarily by the internal boundaries between the inorganic and organic systems; if the local swelling is less significant, the permeability is controlled primarily by the external boundaries. These four

Table 4
Input parameters for experiment conducted by Jin et al. (2015).

Sample	ϕ_{in0}	k_{apin0}	k_{apor0}	E_{in}	ε_L	P_L
Sample BH	0.02	15×10^{-18}[m^2]	1×10^{-19}[m^2]	40[GPa]	0.002	2[MPa]
Sample CH	0.005	3×10^{-18}[m^2]	1×10^{-20}[m^2]	20[GPa]	0.0005	4[MPa]

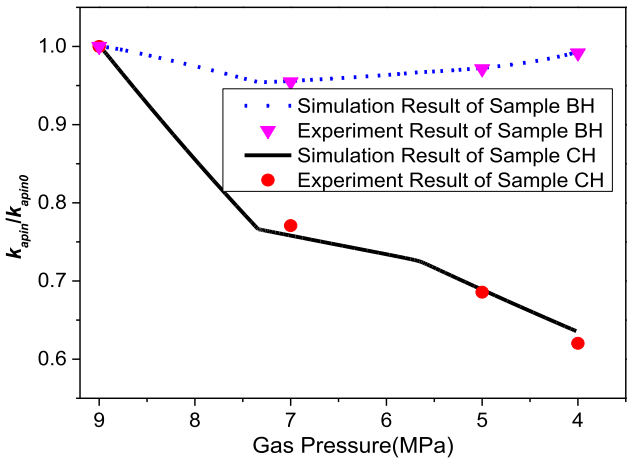

Fig. 9. Comparisons of reproduced result with experimental result for gas desorption processes.

examples represent two end-member behaviors, alternately accentuating local effects or muting local effects. For most cases in reality, the controlling factor may switch gradually from the internal boundaries to the external boundaries.

5. Analysis of field observations

5.1. Model establishment and history matching

In this section, production data from two production wells from both Barnett Shale and Marcellus Shale reservoirs are used for history matching (Al-Ahmadi and Wattenbarger, 2011; Yu and Sepehrnoori, 2014; Yu et al., 2015; Cao et al., 2016). A horizontal well with hydraulic fractures is simulated by a number of shale blocks, which are defined as the shale matrix between hydraulic fractures. Because of the symmetry, one half of the shale block, as illustrated by the red rectangle in Fig. 10, is used for the simulation model. The height of the simulation model is the half-length of the hydraulic fractures and the width is half of the hydraulic fracture spacing (Peng et al., 2015). For the mechanical model, a uniaxial strain condition is assumed: a constant formation pressure is applied on the upper boundary while a roller boundary is set on the other sides. For gas flow in the inorganic system, the extraction pressure is applied on the right side to simulate the pressure change in the hydraulic fracture and no flow boundary conditions are applied on the other boundaries. For the gas flow in the organic pore and kerogen system, no flow boundary conditions are applied as they do not communicate with the hydraulic fractures directly.

Barnett Shale is the main source rock for the Paleozoic petroleum

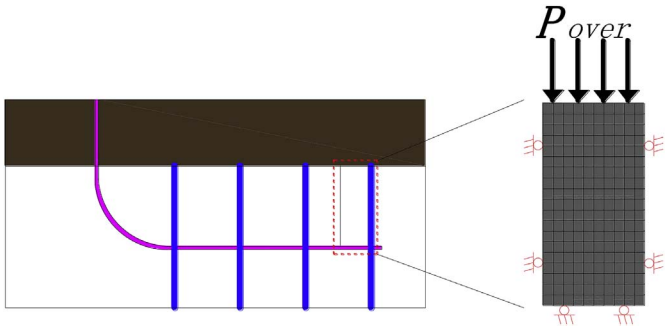

Fig. 10. Illustration of the field simulation model: The purple line represents the horizontal well while the blue lines represent hydraulic fractures. (For interpretation of the references to colour in this figure legend, the reader is referred to the web version of this article.)

Table 5
Properties of the Barnett shale.

'Known' Parameters	Value	'Assumed' Parameters	Value
Initial reservoir pressure (MP_a)	20.3	Young's modulus of Shale(GP_a)	40
Bottom hole pressure (MP_a)	3.45	Initial organic permeability(m^2)	1.5×10^{-22}
Fracture space(m)	30.5	Initial organic porosity	0.04
Fracture half-length(m)	47.2	Kerogen ratio	0.3
Reservoir temperature (°C)	65.6	Kerogen diffusion time(s)	1×10^{9}
Initial inorganic permeability (m^2)	1.5×10^{-19}	Poisson's ratio	0.2
Inorganic matrix porosity	0.06	Langmuir pressure constant (MP_a)	4.48

system in the Fort Worth Basin and is currently one of the most prolific gas reservoirs in the United States (Martineau, 2007). Well 314 was a horizontal well with multi-stage fracturing and with a single, perforated interval for each stage producing at a constant bottom-hole pressure. The hydraulic fracture spacing and half-length were set at 30.5 m and 47.2 m, respectively, and the number of fractures was 28 (Al-Ahmadi and Wattenbarger, 2011; Yu and Sepehrnoori, 2014). More than 1600 days of production data were collected for the history match. The initial gas rate reached ~2.1×10^5 m^3/day but decreased to 1.6×10^4 m^3/day 4.5 years later. Specifically, the average reservoir parameters of the Barnett Shale, collected from the literature (Al-Ahmadi and Wattenbarger, 2011; Yu and Sepehrnoori, 2014), are used for history matching as shown in Table 5. Note that the 'Known' Parameters represent parameter collected from the reservoir or literature and 'Assumed' Parameters represents parameter used for history matching.

Marcellus Shale is a black, middle-Devonian-age sedimentary rock from the Appalachian Basin with very low permeability, typically between 0.1 and 0.00001 mD (Lee et al., 2011). The reservoir comprises two different shale layers with high TOC. The well used for history matching was drilled in the lower section of the Marcellus formation and was hydraulically fractured with a high rate slickwater treatment in 7 stages. Each stage comprises four perforation clusters with a total of 28 hydraulic fractures. The hydraulic fracture spacing and half-length were set at 15.2 m and 121.9 m, respectively (Yu et al., 2015). The bottom hole pressure was calculated based on the work of Yeager and Meyer (2010). Only 250 days of production data are available for the history match. The gas rate ultimately decreased to only 25% of that recorded during the first few days by ~250 days. The reservoir parameters for history matching of the Marcellus Shale are obtained from the literature (Yeager and Meyer, 2010; Yu et al., 2015; Cao et al., 2016) as shown in Table 6.

The comparisons of modeled gas production rate and the accumulative gas production with the field data are shown in Fig. 11. For both cases, the initial gas production rate from the simulation results is larger than the actual field data. This may be due to water flow back reducing the gas production rate (Cao et al., 2016) while the gas will dominate the gas production over the later period of the depletion. Also the skin effect is ignored in our work which results in a lower permeability for the hydraulic fractures. For the case of Barnett Shale, the cumulative gas production obtained from the simulation model is lower than that calculated from field data as shown in Fig. 11 (a). For the case of Marcellus Shale, the gas rate and cumulative gas production obtained from simulation results are in good agreements with those from field data as shown in Fig. 11(b).

In the following sections, the verified model, presented above, is used as a base case model to conduct a series of sensitivity studies. Parameters used for the base case are listed in Table 7. Boundary conditions for the deformation model and the flow model remain unchanged. In addition, a time-dependent pressure (Cao et al., 2016) is

Table 6
Properties of the Marcellus shale.

'Known' Parameter	Value	'Assumed' Parameter	Value
Initial reservoir pressure (MP_a)	34.6	Young's modulus of Shale(GP_a)	50
Bottom hole pressure(MP_a)	3.69	Initial organic permeability(m^2)	2×10^{-20}
Fracture space(m)	15.2	Initial organic porosity	0.045
Fracture half-length(m)	121.9	Kerogen diffusion time (s)	1×10^{7}
Reservoir temperature(°C)	76.1	Kerogen ratio	0.3
Initial inorganic permeability (m^2)	1×10^{-19}	Poisson's ratio	0.2
Inorganic matrix porosity	0.046	Langmuir pressure constant(MP_a)	3.45

applied to simulate the pressure change in the hydraulic fracture during the production process. We assume that the gas in the inorganic system exists as free gas, the gas in the organic pores is a mixture of free and adsorbed gas, and the gas in the kerogen exists only as an adsorbed gas. The proportions of these four components are assumed as 15%, 15%, 5% and 65% in the base model.

5.2. Investigation of interactions between shale components

A shale block sandwiched between hydraulic fractures consists of two systems (organic system and inorganic system) and three gas-bearing components (kerogen, organic pores and inorganic pores). In this section, we change the transport property of one component while the other two remain unchanged. This allows a study of key sensitivities.

5.2.1. Impact of the inorganic system

The inorganic system stores free gas and acts as a bridge connecting the organic system to the hydraulic fracture. We increase the permeability of the inorganic system from 1×10^{-21} to 5×10^{-19} m^2 to investigate how the gas recovery rate changes with results shown in Fig. 12.

As shown in Fig. 12, the recovery rate increases with the permeability of the inorganic system. The gas recovery rate after 30 years for the case of the lowest inorganic permeability (5×10^{-21} m^2) is about 40% of that for the case of the highest permeability (5×10^{-19} m^2). However the incremental increase of recovery rate is not directly proportional to the permeability increase when the permeability is high, as shown in Fig. 12 (b). The recovery rate increases linearly as the permeability increases from 1×10^{-21} m^2 to 1×10^{-19} m^2 but remains almost flat when the inorganic permeability is larger than 5×10^{-19} m^2. This result implies that the gas recovery rate is not controlled by the flow capability of the inorganic system, but rather by the mass supply of gas from the organic system and that the limiting process can switch from gas flow in the inorganic system to gas diffusion in the organic system.

Fig. 13 shows the evolution of gas production rate for different permeabilities. In general, the initial high gas production rates decrease rapidly in the first years and then remain flat. For an inorganic permeability of 5×10^{-19} m^2, the flow rate reaches ~5×10^3 m^3/day initially then drops to 0.1 m^3/day in five years. This is because (1) at early time the flow rate is determined by the permeability of the inorganic system; (2) as the initial high flow rate diminishes, the flow rate

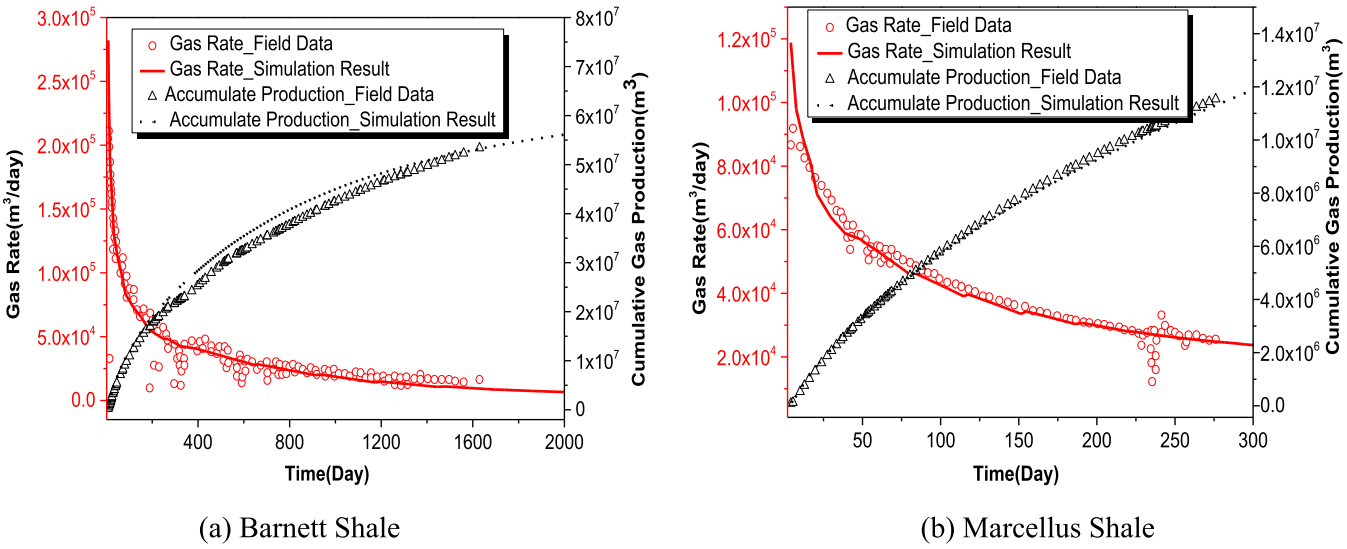

Fig. 11. History matching for two field cases.

Table 7
Parameters of the base model.

Parameter	Value	Parameter	Value
Gas density(kg/m^3)	0.714	Organic Pores intrinsic permeability(m^2)	1.25×10^{-21}
Dynamic viscosity(P_a•s)	2×10^{-5}	Kerogen ratio	0.25
Langmuir pressure constant(MP_a)	10	Diffusion time in kerogen (s)	2.5×10^{9}
Langmuir volume constant(m^3/kg)	0.0022	Atmosphere pressure(MP_a)	0.1
Temperature(°C)	50	Initial pressure(MP_a)	40
Shale gas molecule diameter (nm)	0.38	Biot's coefficient of kerogen	0.4
Inorganic system intrinsic permeability(m^2)	1.5×10^{-19}	Biot's coefficient of pores in organic matter	0.4
Radius of inorganic pores(nm)	100	Young's modulus of shale(GP_a)	20
Langmuir strain constant	0.024	Poisson's ratio of shale	0.2
Shale density(kg/m^3)	2500	Biot's coefficient of inorganic system	0.4

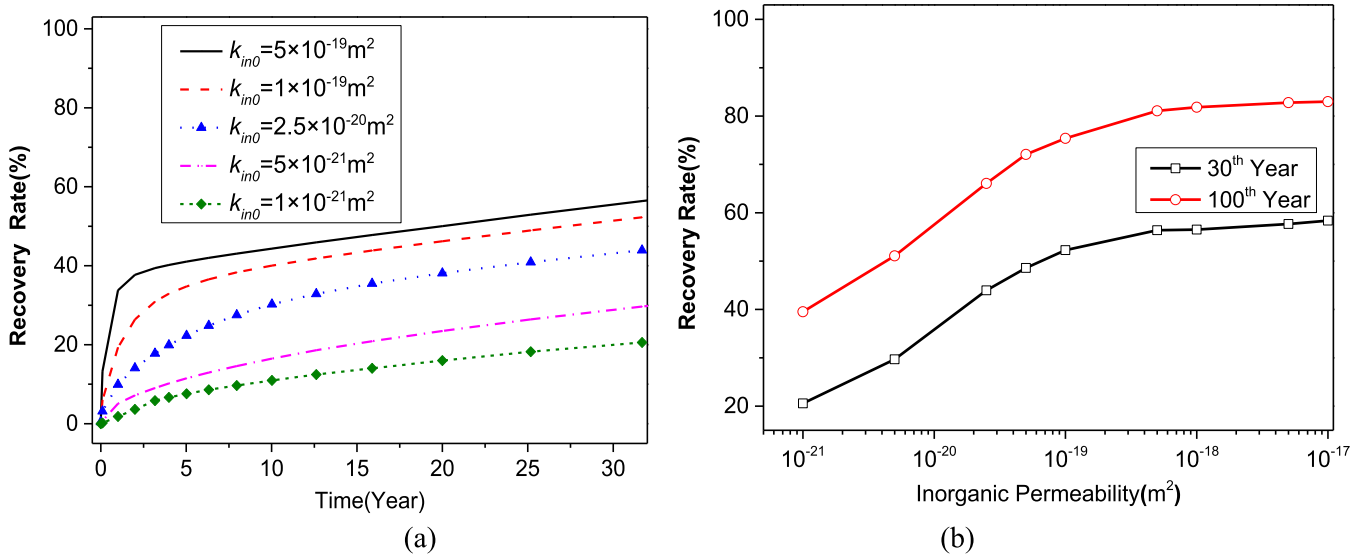

Fig. 12. (a) Evolution of gas recovery rates under different magnitudes of permeability in the inorganic system; (b) Impact of permeability magnitudes on the recovery rate.

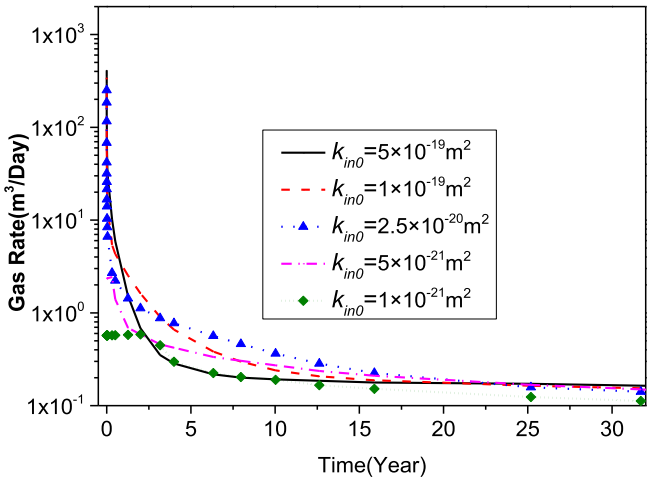

Fig. 13. Gas production rates under different magnitudes of permeability in the inorganic system.

is then controlled by the gas supply from the organic system.

5.2.2. *Impact of organic pores*

We now change the permeability of the organic pores and see how this change affects the gas recovery rate. Fig. 14 (a) represents the evolution of gas recovery rate under different magnitudes of organic pore permeability. Fig. 14 (b) shows that the recovery rate increases with the permeability and the recovery rate also increases with the organic pore permeability. This increase exhibits three stages: (1) The increased permeability has little impact on the recovery rate when the permeability is lower than $\sim 1 \times 10^{-20}$ m^2. Under this situation, the gas production process is limited by gas diffusion from the organic system to the inorganic system not by the flow process in the inorganic system; (2) The gas recovery rate increases linearly with the organic pore permeability when the permeability ranges from 1×10^{-20} to 2.5×10^{-19} m^2. In this situation, the gas production is limited by the flow process in the inorganic system; and finally, (3) The gas production becomes stable when the organic pore permeability continues to increase and becomes larger than the inorganic system (unrealistic in reality) as shown by the black dashed line in Fig. 14. Under this si-

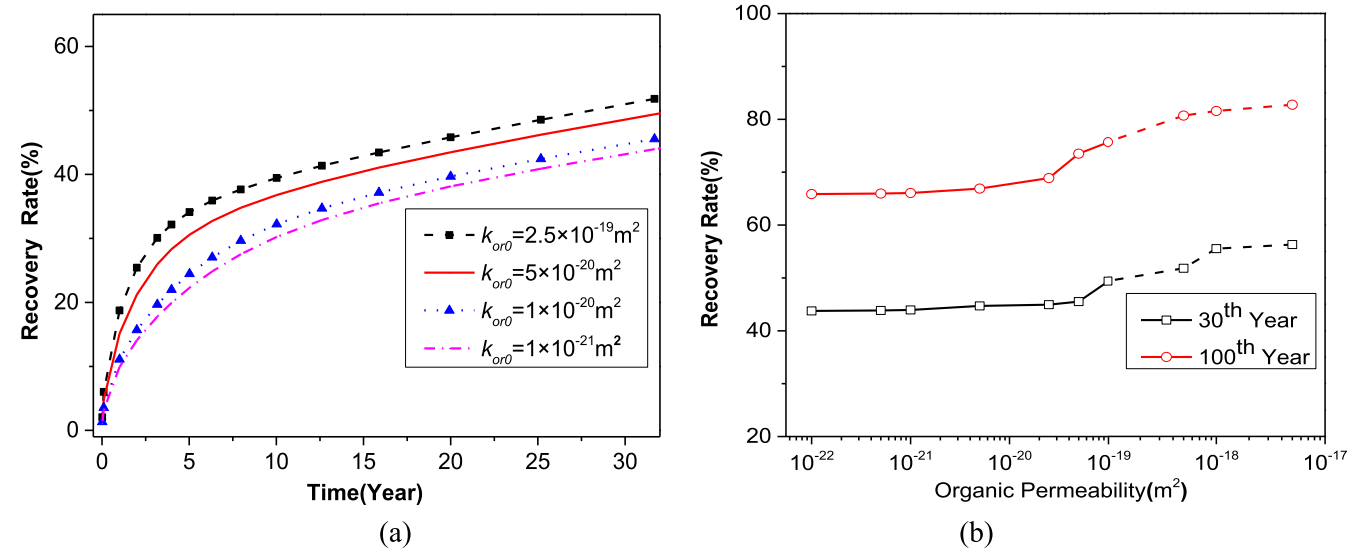

Fig. 14. (a) Evolution of gas recovery rates under different magnitudes of inorganic system permeability; (b) Relation between gas recovery rate and permeability under different production years.

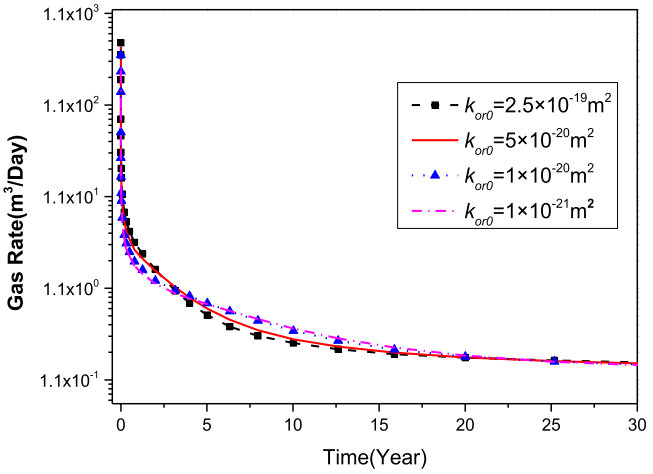

Fig. 15. Evolution of gas production rates under different magnitudes of organic pore permeability.

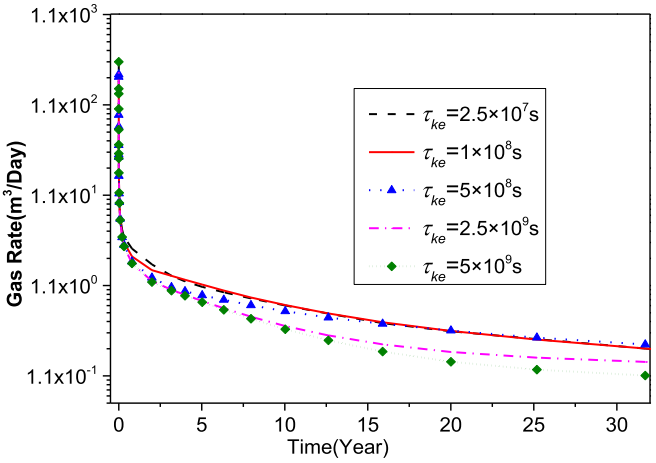

Fig. 17. Evolution of gas production rate under different magnitudes of diffusion time.

tuation, the gas production process is limited either by the gas diffusion in the kerogen or by the low permeability in the inorganic system.

Fig. 15 shows the evolution of gas production rate under different magnitudes of organic pore permeability. It can be seen that the magnitudes of organic pore permeability have almost no impact on the initial gas production rate. As shown in Fig. 15, the initial flow rates under different magnitudes of permeability are about 1.5 × 10^3 m^3/day. This is because the initial high flow rate is determined primarily by the permeability of the inorganic system.

5.2.3. Impact of kerogen

In this part, we change the diffusion time for the kerogen component. Fig. 16 shows the evolution of gas recovery rate under different magnitudes of diffusion time. As shown in Fig. 16 (a), the impact of diffusion time on the gas recovery rate diminishes as it decreases. This result implies that when the diffusion time is larger, the gas production process is diffusion limited; when the diffusion time is smaller, the limiting process switches from diffusion in the kerogen to the flow processes in the inorganic system. As shown in Fig. 16 (b), the gas recovery rate increases significantly when the diffusion time is larger. In this situation, gas production is limited by the diffusion process in the kerogen. The gas recovery rate becomes near constant at small diffusion times. In this situation, the rate limiting process switches from diffusion in the kerogen to flow processes in the inorganic system.

Fig. 17 shows the evolution of gas production rate under different magnitudes of diffusion time. The diffusion time has almost no impact on the initial gas production rate because the initial rate is primarily determined by the permeability of the inorganic system. The enhanced diffusion rate in the kerogen increases the gas rate at late time and smooths the decline curve of gas rate. As the diffusion time decreases, its impact on the gas production rate also diminishes.

As shown above, the rate limiting process for gas production may switch between gas supply processes and gas flow processes when we change the transport properties of one of three gas-bearing components (kerogen, organic pores and inorganic pores). This is because this change enhances the contrast in transport properties between components. In this situation, the time to reach an equilibrium pressure between components would be extended. We retain the contrast unchanged and introduce a ratio, η, to represent the enhancement of the shale block transport properties as defined as $\eta = K_{ch}/K_{in}$, where K_{ch} is the new transport property and K_{in} is the initial property. Fig. 18 shows the evolution of gas recovery rate under different magnitudes of η. The model results show that the gas recovery rate increases with the magnitude of η. This implies that there would be no switch of the limiting

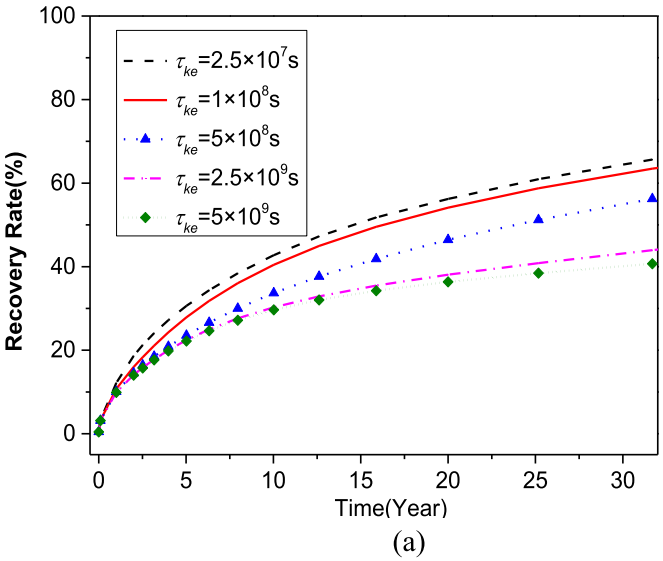

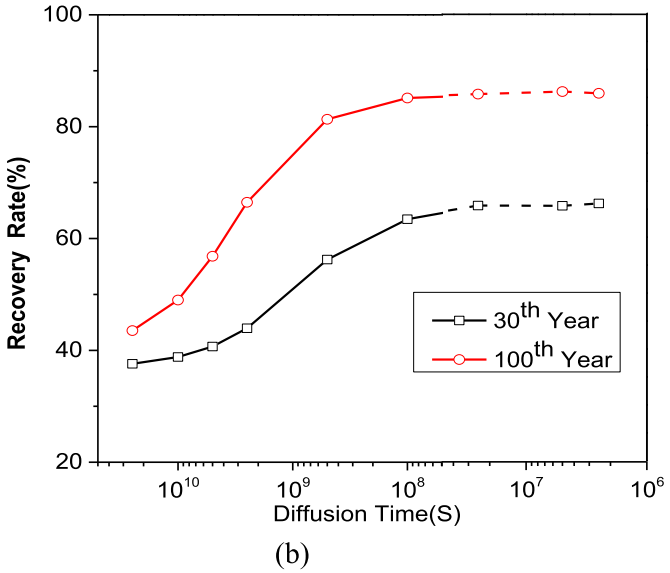

Fig. 16. (a) Evolution of gas recovery rate under different magnitudes of diffusion time; (b) Relation between gas recovery rate and diffusion time for a specific production time.

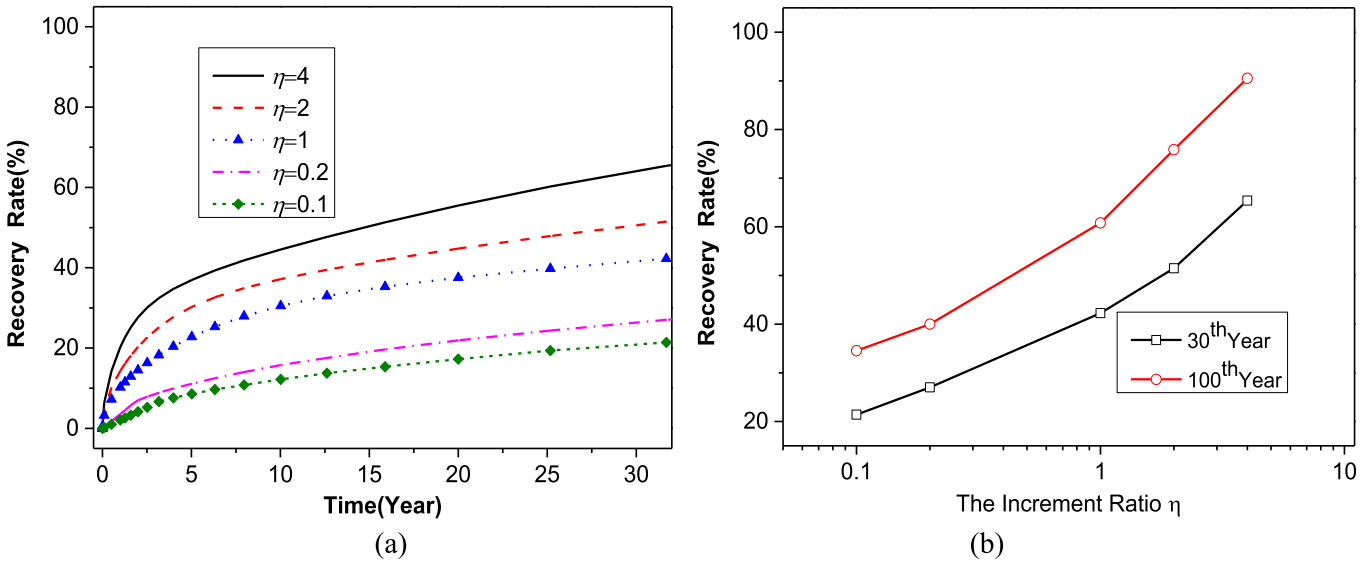

Fig. 18. (a) Evolution of gas recovery rate under different magnitudes of the enhancement ratio; (b) Relation between gas recovery rate and the property enhancement ratio.

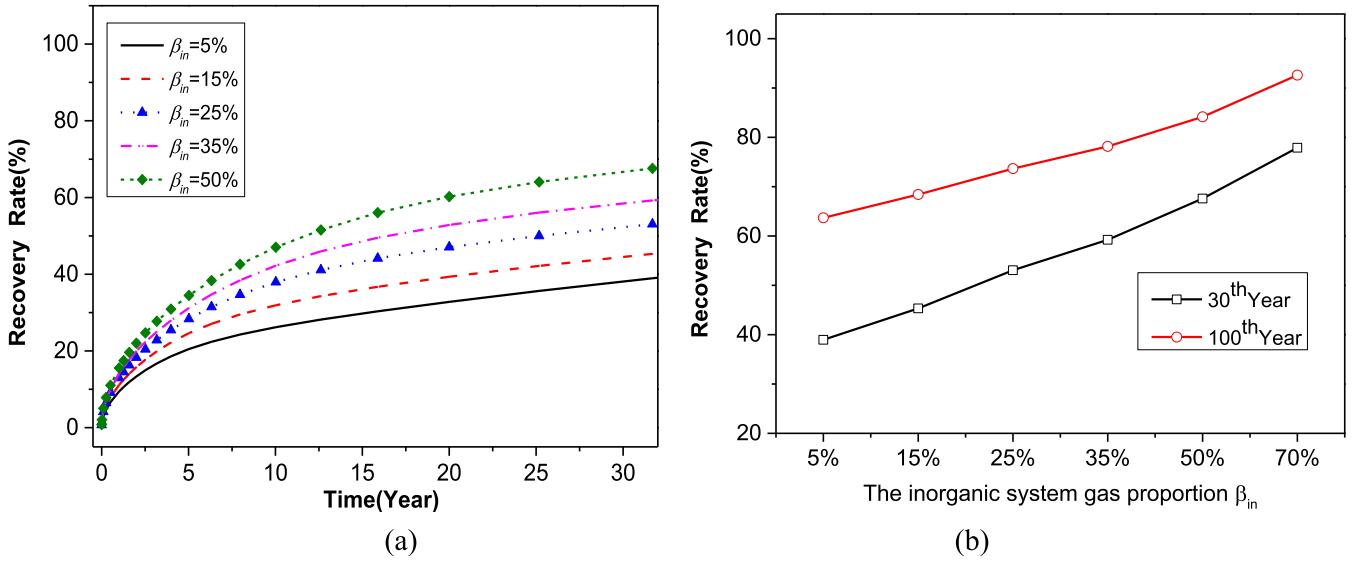

Fig. 19. (a) Evolution of gas recovery rate under different magnitudes of the gas ratio; (b) Relation between the gas recovery rate and the initial gas ratio.

process between gas supply and gas flow if the contrast of the transport properties was not modified.

5.3. Impact of initial gas distribution

If we now change the ratio of gas in the inorganic system, β_{in}, to gas in the organic system, β_{or}, to investigate how this ratio affects the gas recovery rate. The summation of these two components are unity, $\beta_{in}+\beta_{or} = 1$. As shown in Fig. 19 (a), the gas recovery rate increases almost linearly with the ratio of initial gas in the inorganic system. The recovery rate is only 35% over 30 years when 5% gas is in the inorganic system while this recovery becomes 65% when the gas in the inorganic system changes from 5% to 50%. Fig. 19 (b) also shows that the gas recovery rate increases almost linearly with the magnitudes of the gas ratio in the inorganic system. Fig. 20 shows the gas rates with different magnitude of gas ratio in the inorganic system. It shows that the decline is smoother when more gas is stored in the inorganic system. To the contrary, the larger gas ratio in the organic system leads to a sharper decline in the gas rate. These characteristics are due to the fact that the

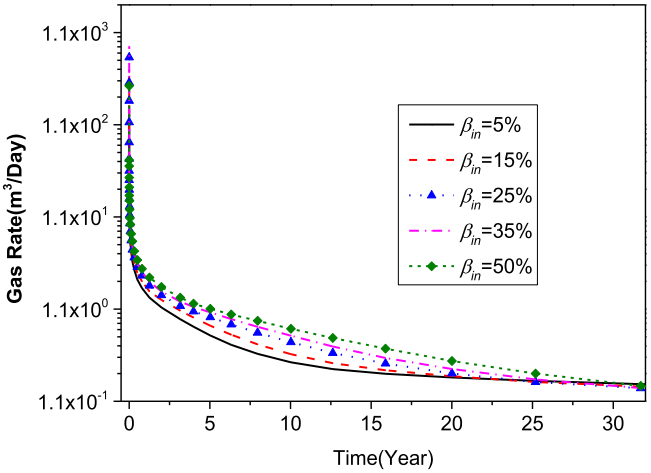

Fig. 20. Evolution of gas production rate under different magnitudes of β_{in}.

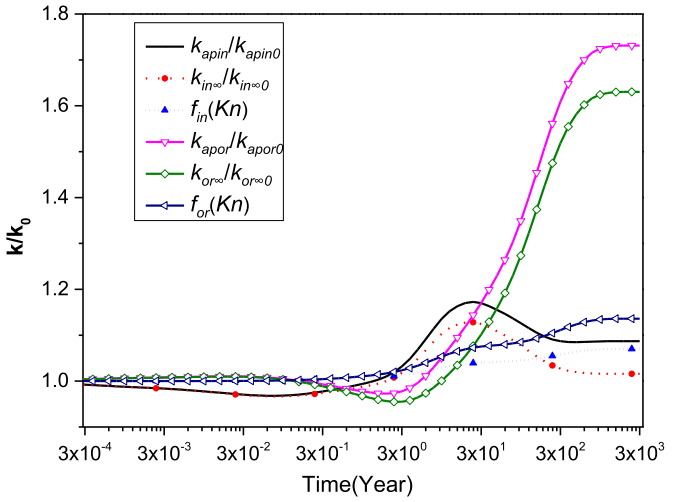

Fig. 21. Evolution of intrinsic permeability, apparent permeability, and correlation factor of inorganic system and organic system.

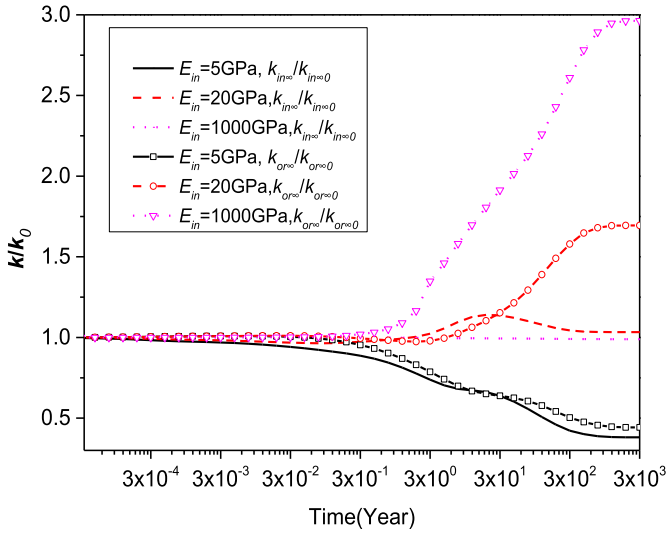

Fig. 22. Evolution of intrinsic permeability of inorganic system and organic system.

contrasts in storage properties of the two systems become larger and the inorganic system connects to the hydraulic fractures directly which is characterized by a high flow rate.

5.4. Evolution of permeability

We now investigate how the intrinsic permeability and the apparent permeability evolve during the gas production process. Fig. 21 illustrates the evolution of the apparent permeability, the intrinsic permeability and the correction factors for both systems. For the inorganic system, four distinctive stages of permeability evolution are observed: A Decreasing Stage (the first 100 days), An Increasing Stage (from 100 days to 30 years), A Recovery Stage (from 30 years to 300 years) and A Stable Stage. For the organic system, the four stages can also be seen: An Increasing Stage (the first 3 days), A Decreasing Stage (from 3 days to 3 years), A Recovery Stage (from 3 years to 300 years) and A Stable Stage. In the first three years, the permeability of the inorganic system decreases slightly then rebounds to the initial value while the permeability of the organic system increases slightly then decreases to a minimum value. During this process, the production rate experiences a sharp decrease as the contrasts in transport properties of the two systems become accentuated. Congruent with the discussion above, an increased contrast in the transport and gas storage properties of the two systems results in a faster recovery decline of a shale well.

We use the evolution of permeability in the inorganic system as an example to illustrate why these four stages result. Prior to gas production, the shale is at equilibrium state. As the gas production proceeds, a series of processes take place. The gas in the micro-fractures flows out first because of the relatively high permeability. As a result of this process, the gas pressure in the micro-fractures decreases and a pressure difference between the inorganic system and the organic system is created. Under this situation, the micro-fractures are compressed. Because this happens only locally, in the vicinity of micro-fractures, this compression reduces the permeability. This is why we see an initial stage of permeability decrease at early time. Because of the pressure difference between the micro-fractures in the inorganic and organic systems, the gas in the organic system diffuses into the micro-fractures. Under this condition, the organic system shrinks while the micro-fractures swell. Because this also happens locally in the vicinity of the micro-fractures, the shrinking volume of the organic system may be equal to the swelling volume of the micro-fracture. This is why we see the second stage of permeability increase. As the gas pressure difference extends further into the organic system, the gas pressure decreases in the whole organic system until a new equilibrium state is reached between the two systems. Because this happens globally throughout the system, the whole matrix system shrinks as do the micro-fractures. This is why we see the third stage of permeability recovery (before the new equilibrium state) and the fourth stage of permeability stabilization (after the new equilibrium state).

5.5. Impact of shale deformability

In this part, we change the magnitude of the Young's modulus of the inorganic system to investigate how the permeability evolves. We change the magnitude of the modulus from the 5 GPa to an unrealistically high 1000 GPa. The evolutions of the intrinsic permeabilities of the two systems are shown in Fig. 22. When the inorganic system is rigid (E_{in} = 1000 GPa), the permeability of the inorganic system remains unchanged while the permeability of the organic system changes the most. When the inorganic system is deformable (E_{in} = 5 GPa), the permeabilities of both systems decrease.

6. Conclusions

In this study, the inconsistency between the observed evolution of shale permeability and the effective stress principle is resolved through incorporating matrix-fracture interactions into both matrix and fracture permeability models. These models are the key cross-relations that couple the shale deformation and gas flow, and define the interfacial dynamics between two distributed components (inorganic and organic systems). The coupled model follows how the interfacial dynamics affects the evolution of shale permeability and gas production rate. Based on model results, the following conclusions are drawn:

(1) The evolution of shale permeability is controlled by the interfacial dynamics between the inorganic and organic components. The impact of the interfacial dynamics is determined by contrasts in the transport and deformation properties between these two components. If the contrasts are significant, the interfacial dynamics dominate the evolution of shale permeability while the outer boundaries have less impact. If the contrasts are less significant, the outer boundaries determine the evolution of shale permeability while the inner boundaries have less impact. The early evolution of permeability is primarily due to internal behavior in the gas invaded-region within the inorganic system while the later evolution is due to the global deformation as the gas pressure or the effective stress propagates further into the organic component.
(2) The shale gas production rate is also controlled by the interfacial

dynamics between the inorganic and organic components. The impact of the interfacial dynamics is determined by contrasts in transport, gas storage and deformation properties between these two components. If the contrasts are significant, the interfacial dynamics dominate the evolution of shale gas production rate while the outer boundaries have less impact. If the contrasts are less significant, the outer boundaries determine the evolution of gas production rate while the inner boundaries have less impact. The pore network in the inorganic system significantly impacts the early productivity of the shale reservoir while the diffusion in the organic component (kerogen) plays a decisive role in the long-term production.

Acknowledgements

This work was funded partially by Natural Science Foundation of China (51504235; 51474204), and the 111 Project (B17009). These supports are gratefully acknowledged. The authors would also like to thank all anonymous reviewers for their constructive comments.

References

Akkutlu, I.Y., Fathi, E., 2012. Multiscale gas transport in shales with local kerogen heterogeneities. Spe J. 17 (4), 1002–1011.
Al-Ahmadi, H.A., Wattenbarger, R.A., 2011. Triple-porosity models: one further step towards capturing fractured reservoirs heterogeneity. In: SPE/DGS Saudi Arabia Section Technical Symposium and Exhibition. Society of Petroleum Engineers.
Ambrose, R.J., Hartman, R.C., Campos, M.D., et al., 2010. New pore-scale considerations for shale gas in place calculations. In: SPE Unconventional Gas Conference. Society of Petroleum Engineers..
Bai, B., Elgmati, M., Zhang, H., et al., 2013. Rock characterization of Fayetteville shale gas plays. Fuel 105 (3), 645–652.
Boitnott, G.N., 1997. Use of complex pore pressure transients to measure permeability of rocks. In: PE Annual Technical Conference and Exhibition. Society of Petroleum Engineers.
Brace, W.F., Walsh, J.B., Frangos, W.T., 1968. Permeability of granite under high pressure. J. Geophys. Res. 73 (6), 2225–2236.
Bumb, A.C., McKee, C.R., 1988. Gas-well testing in the presence of desorption for coalbed methane and devonian shale. SPE Form. Eval. 3 (01), 179–185.
Bustin, R.M., Bustin, A.M.M., Cui, A., et al., 2008. Impact of shale properties on pore structure and storage characteristics. In: SPE Shale Gas Production Conference. Society of Petroleum Engineers.
Cao, P., Liu, J.S., Leong, Y.K., 2016. A fully coupled multiscale shale deformation-gas transport model for the evaluation of shale gas extraction. Fuel 178, 103–117.
Carey, J.W., Lei, Z., Rougier, E., Mori, H., et al., 2015. Fracture-permeability behavior of shale. J. Unconv. Oil Gas Resour. 11, 27–43.
Chen, C., Hu, D., Westacott, D., et al., 2013a. Nanometer-scale characterization of microscopic pores in shale kerogen by image analysis and pore-scale modeling. Geochem. Geophys. Geosys. 14 (14), 4066–4075.
Chen, Z.W., Liu, J.S., Elsworth, D., et al., 2013b. Roles of coal heterogeneity on evolution of coal permeability under unconstrained boundary conditions. J. Nat. Gas Sci. Eng. 15 (6), 38–52.
Chen, D., Pan, Z., Ye, Z., 2015a. Dependence of gas shale fracture permeability on effective stress and reservoir pressure: model match and insights. Fuel 139, 383–392.
Chen, F., Duan, Y., Wang, K., et al., 2015b. A novel pressure transient response model considering multiple migration mechanisms in shale gas reservoir. J. Nat. Gas Sci. Eng. 22 (22), 321–334.
Chen, T.Y., Feng, X.T., Pan, Z.J., 2015c. Experimental study of swelling of organic rich shale in methane. Int. J. Coal Geol. 150–151, 64–73.
Civan, F., 2009. Effective correlation of apparent gas permeability in tight porous media. Transp. Porous Media 82 (2), 375–384.
Curtis, M.E., Cardott, B.J., Sondergeld, C.H., et al., 2012. Development of organic porosity in the Woodford Shale with increasing thermal maturity. Int. J. Coal Geol. 103 (23), 26–31.
Florence, F.A., Rushing, J., Newsham, K.E., et al., 2007. Improved permeability prediction relations for low permeability sands. In: Rocky Mountain Oil & Gas Technology Symposium. Society of Petroleum Engineers.
Guo, C., Xu, J., Wu, K., et al., 2015. Study on gas flow through nano pores of shale gas reservoirs. Fuel 143, 107–117.
Haghshenas, B., Clarkson, C.R., Chen, S., 2013. Multi-porosity, multi-permeability models for shale gas reservoirs. In: SPE Unconventional Resources Conference Canada. Society of Petroleum Engineers.
Heid, J.G., McMahon, J.J., Nielsen, R.F., et al., 1950. Study of the permeability of rocks to homogeneous fluids. In: Drilling and Production Practice. American Petroleum Institute.
Heller, R., Zoback, M., 2014. Adsorption of methane and carbon dioxide on gas shale and pure mineral samples. J. Unconv. Oil Gas Resour. 8, 14–24.
Ho, T.A., Criscenti, L.J., Wang, Y., 2016. Nanostructural control of methane release in kerogen and its implications to wellbore production decline. Sci. Rep. 6, 28053.
Hudson, J.D., Civan, F., Michel, G., et al., 2012. Modeling multiple-porosity transport in gas-bearing shale formations. In: SPE Latin America and Caribbean Petroleum Engineering Conference. Society of Petroleum Engineers.
Javadpour, F., 2009. Nanopores and apparent permeability of gas flow in mudrocks (shales and siltstone). J. Can. Petrol. Technol. 48 (8), 16–21.
Javadpour, F., Fisher, D., Unsworth, M., 2007. Nanoscale gas flow in shale gas sediments. J. Can. Petrol. Technol. 46 (10), 55–61.
Jin, G., Pérez, H.G., Agrawal, G., et al., 2015. The impact of gas adsorption and composition on unconventional shale permeability measurement. In: SPE Middle East Oil & Gas Show and Conference. Society of Petroleum Engineers.
Jones, F.O., Owens, W.W., 1980. A laboratory study of low-permeability gas sands. J. Petrol. Technol. 32 (09), 1631–1640.
Kazemi, M., Takbiri-Borujeni, A., 2015. An analytical model for shale gas permeability. Int. J. Coal Geol. 146, 188–197.
Klinkenberg, L.J., 1941. The permeability of porous media to liquids and gases. In: Drilling and Production Practice. American Petroleum Institute.
Kumar, H., Elsworth, D., Liu, J., et al., 2012. Optimizing enhanced coalbed methane recovery for unhindered production and CO2 injectivity. Int. J. Greenh. Gas Control 11 (6), 86–97.
Kumar, H., Elsworth, D., Mathews, J.P., et al., 2015. Permeability evolution in sorbing media: analogies between organic-rich shale and coal. Geofluids 16 (1), 43–55.
Lee, D.S., Herman, J.D., Elsworth, D., et al., 2011. A critical evaluation of unconventional gas recovery from the marcellus shale, northeastern United States. KSCE J. Civ. Eng. 15 (4), 679–687.
Lee, T., Bocquet, L., Coasne, B., 2016. Activated desorption at heterogeneous interfaces and long-time kinetics of hydrocarbon recovery from nanoporous media. Nat. Commun. 7, 11890.
Li, D., Xu, C., Wang, J.Y., et al., 2014. Effect of Knudsen diffusion and Langmuir adsorption on pressure transient response in tight- and shale-gas reservoirs. J. Petrol. Sci. Eng. 124, 146–154.
Lim, K.T., Aziz, K., 1995. Matrix-fracture transfer shape factors for dual-porosity simulators. J. Petrol. Sci. Eng. 13 (3–4), 169–178.
Liu, J., Wang, J., Chen, Z., et al., 2011. Impact of transition from local swelling to macro swelling on the evolution of coal permeability. Int. J. Coal Geol. 88 (1), 31–40.
Martineau, D.F., 2007. History of the newark east field and the Barnett shale as a gas reservoir. Aapg Bull. 91 (4), 399–403.
Mehmani, A., Prodanović, M., Javadpour, F., 2013. Multiscale, multiphysics network modeling of shale matrix gas flows. Transp. Porous Media 99 (2), 377–390.
Mulder, J., 1996. Basic Principles of Membrane Technology. Springer.
Naraghi, M.E., Javadpour, F., 2015. A stochastic permeability model for the shale-gas systems. Int. J. Coal Geol. 140, 111–124.
Peng, Y., Liu, J., Wei, M.Y., Pan, Z.J., et al., 2014. Why coal permeability changes under free swellings: new insights. Int. J. Coal Geol. 133, 35–46.
Peng, Y., Liu, J.S., Pan, Z.J., et al., 2015. A sequential model of shale gas transport under the influence of fully coupled multiple processes. J. Nat. Gas Sci. Eng. 27, 808–821.
Saghafi, A., Faiz, M., Roberts, D., 2007. CO2 storage and gas diffusivity properties of coals from Sydney Basin, Australia. Int. J. Coal Geol. 70 (1–3), 240–254.
Sakhaee-pour, A., Bryant, S.L., 2011. Gas permeability of shale. In: SPE Annual Technical Conference and Exhibition. Society of Petroleum Engineers.
Sampath, K., Keighin, C.W., 1982. Factors affecting gas slippage in tight sandstones of cretaceous age in the uinta basin. J. Petrol. Technol. 34 (11), 2715–2720.
Sherman, F.S., 1969. The transition from continuum to molecular flow. Annu. Rev. Fluid Mech. 1 (1), 317–340.
Shi, M., Yu, B., Xue, Z., Wu, J., et al., 2015. Pore characteristics of organic-rich shales with high thermal maturity: a case study of the Longmaxi gas shale reservoirs from well Yuye-1 in southeastern Chongqing, China. J. Nat. Gas Sci. Eng. 26 (4), 948–959.
Siriwardane, H., Haljasmaa, I., Mclendon, R., et al., 2009. Influence of carbon dioxide on coal permeability determined by pressure transient methods. Int. J. Coal Geol. 77 (1–2), 109–118.
Vafaie, A., Habibnia, B., Moallemi, S.A., 2015. Experimental investigation of the pore structure characteristics of the Garau gas shale formation in the Lurestan Basin, Iran. J. Nat. Gas Sci. Eng. 27 (4), 432–442.
Wang, J.G., Kabir, A., Liu, J., et al., 2012. Effects of non-Darcy flow on the performance of coal seam gas wells. Int. J. Coal Geol. 93 (1), 62–74.
Wang, K., Zang, J., Wang, G., et al., 2014. Anisotropic permeability evolution of coal with effective stress variation and gas sorption: model development and analysis. Int. J. Coal Geol. 130 (4), 53–65.
Wasaki, A., Akkutlu, I.Y., 2014. Permeability of organic-rich shale. In: SPE Annual Technical Conference and Exhibition. Society of Petroleum Engineers.
Wu, Y., Liu, J., Chen, Z., et al., 2011. A dual poroelastic model for CO2-enhanced coalbed methane recovery. Int. J. Coal Geol. 86 (2–3), 177–189.
Yang, B., Kang, Y., You, L., et al., 2016. Measurement of the surface diffusion coefficient for adsorbed gas in the fine mesopores and micropores of shale organic matter. Fuel 181, 793–804.
Yeager, B.B., Meyer, B.R., 2010. Injection/Fall-off testing in the marcellus shale: using reservoir knowledge to improve operational efficiency. In: SPE Eastern Regional Meeting. Society of Petroleum Engineers.
Yu, W., Sepehrnoori, K., 2014. Simulation of gas desorption and geomechanics effects for unconventional gas reservoirs. Fuel 116 (1), 455–464.
Yu, W., Zhang, T.T., Du, S., et al., 2015. Numerical study of the effect of uneven proppant distribution between multiple fractures on shale gas well performance. Fuel 142, 189–198.
Zhang, H.B., Liu, J.S., Elsworth, D., 2008. How sorption-induced matrix deformation affects gas flow in coal seams: a new FE model. Int. J. Rock Mech. Min. Sci. 45 (8), 1226–1236.
Zhang, L., Li, D., Li, L., et al., 2014. Development of a new compositional model with multi-component sorption isotherm and slip flow in tight gas reservoirs. J. Nat. Gas Sci. Eng. 21, 1061–1072.